Modelling Aerothermal Heating with Conjugate Heat Transfer

by

Imthiaz Syed

A thesis
presented to the University of Waterloo
in fulfillment of the
thesis requirement for the degree of
Masters of Applied Science
in
Mechanical Engineering

Waterloo, Ontario, Canada, 2021

Author's Declaration

I hereby declare that I am the sole author of this thesis. This is a true copy of the thesis, including any required final revisions, as accepted by my examiners.

I understand that my thesis may be made electronically available to the public.

Abstract

Supersonic and hypersonic vehicles experience flows under complex thermodynamic conditions due to the presence of shock waves and large thermophysical gradients. A large thermal load is imparted to the vehicle from the high-speed flow, leading to the aerodynamic heating of the surface. Additionally, the vehicle must sustain heat loads from within its structure, such as the propulsion system. The accurate modelling of heat transfer at these highly non-adiabatic wall conditions is critical in designing optimal thermal protection systems for hypersonic vehicles. This thesis aims to assess the predictive capabilities of computational fluid dynamic solvers in modelling aerothermal heating in supersonic and hypersonic flows using Conjugate Heat Transfer (CHT) methodologies, and investigate the impact of internal heating sources on the thermal and aerodynamic loads on aerospace vehicles. The predictive capabilities of near-wall turbulence modelling at high-speed, non-adiabatic flow conditions are first assessed for two commercial and two open-source CFD solvers: OpenFOAM (open-source), SU2 (open-source), Star-CCM+ (commercial), and ANSYS CFX (commercial). The overall error and uncertainty that can be attributed to solver selection at these complex conditions is quantified. SU2 and Star-CCM+ are assessed on their ability to model aerodynamic heating using CHT, with comparisons to hypersonic experimental studies and prior numerical investigations. The results from the code validations are used as a basis to conduct a CHT analysis on a simplified model of a supersonic vehicle to investigate the impact of internal heating on the thermal boundary layer of the external flow. The results show notable variations between the solvers in the kinematic and thermodynamic profiles of the high-speed non-adiabatic boundary layers, which are quantified. Furthermore, the treatment of the boundary condition at the wall plays a significant role in the variation of wall properties, particularly with the wall temperature prediction. Moreover, CHT validation studies show that aerothermal heating predictions of current commercial and open-source CHT solvers agree well with experimental and numerical data, but significant prediction errors occur in regions of Shockwave Boundary Layer Interaction (SWBLI) and stagnation points. The addition of internal heating on the CHT simulations of the generic high-speed vehicle results in a reversal of the wall heat flux vector as the freestream Mach Number is increased, where the heated wall case at low supersonic speeds transforms to a cooled wall case at hypersonic speeds. This thesis work provides a solid groundwork for conducting CHT simulations of high-speed wall-bounded flows with internal heating, using RANS solvers.

Acknowledgements

I would first like to thank my supervisor, Dr. Jean-Pierre Hickey, whose guidance and expertise was indispensable to phrasing the research problem and the breakdown of research milestones. Jean-Pierre, your feedback helped me stay on track and made me experiment with novel research ideas, and ultimately allowed me to tie up the entire research together. I thank you also for your consistent assistance in providing the tools necessary for my research, and ever-willingness to offer a hand when I was struggling. I thank you also for all of the opportunities you have given me to further my research and career.

I'd like to thank my coworkers and colleagues at QinetiQ Target Systems (QTS), with whom I conducted a majority of my research alongside. I'd like to particularly thank Byran Godbolt for the opportunity that he has given me. It is incredibly hard to get an opportunity which lines up so nicely with my research and career endeavors, and I am ever grateful for it. I'd like to also thank Dale Mckay, Garrett Gustafson, and Ed Farnfield for their patience, support and guidance during my stay in Alberta.

I would also like to acknowledge my peers and colleagues from the Multi-Physics Interactions Lab. I would particularly like to thank my friends and peers, Alex Bukva and Khaled Younes for their ever-helping attitude, without which the courses I took would have been such a tedium. You both provided me with a place of respite, where we could relate with each other going through similar programs and research topics. I would also like to thank Hamid Mohammad, Nicholas Christopher, and Jeremy Wang, who provided me with critical snippets of knowledge along the way, allowing me to breeze through the learning the fundamentals of high-speed flows.

I would also like to thank Robbie Edwards, who kick-started this whole ride. Who knew a casual talk about rockets over lunch would provide me with the opportunity to actually research them. I really don't think I'd be where I am currently without our conversation back then, as well as your recommendation. As such, I also want to thank Dr. Alexander Jablonski, for the opportunity to conduct research at the Canadian Space Agency, which gave me the initial spark to pursue a Masters degree.

Thank you.

Dedication

This is dedicated to my parents Abid and Naveen, and my sister Amanee. Thank you for always being there for me, through the highest of highs and the lowest of the lows. This is also dedicated to my Grandpa, who kept telling me, year after year, from the day I was born to today, that I will be a rocket scientist. I may not be there yet, but here's the first step.

Table of Contents

List of Figures

List of Tables

Chapter 1

Introduction

A viscous fluid flowing over a solid body adheres to the surface and generates a boundary layer [5]. Compression and deceleration of the flow at the surface converts the kinetic energy of the fluid into thermal energy. Further heating is generated by frictional forces at the fluid-solid boundary. Together, these thermal loads constitute aerodynamic heating [6]. At low speeds, this thermal effect is not of concern for general aerodynamic problems, especially considering the much lower density of air at higher altitudes. However, vehicles moving at supersonic and hypersonic speeds through the atmosphere during their ascent and cruise phases of flight or during atmospheric re-entry experience significant aerodynamic heating [6]. A large thermal load is imparted to the high-speed vehicle.

Aerodynamic heating depends on several factors, including vehicle orientation and flow condition [4]. Predictive simulations of high-speed aerospace vehicles depend on an accurate modelling of the relevant physics of the problem. Since the scales of the turbulent activity within the boundary layer span many orders of magnitude and vary in both space and time, most engineering-level computational fluid dynamics (CFD) simulations rely on Reynolds-Averaged Navier–Stokes (RANS) turbulence models to reduce computational costs [5]. As the fluid at these conditions experiences large density and temperature gradients, the compressible form (Favre-averaged) of the RANS equations is used [5]. However, several simplifications are made in the implementation of the Favre-averaged RANS equations in CFD codes that may break down in high-speed flows, particularly in flows with large temperature gradients, and more specifically, in shock-wave-boundary layer interactions.

As many high-speed flows occur under complex thermodynamic conditions, especially in the hypersonic regime, the walls are often at non-adiabatic conditions where accurate

heat transfer modelling is essential. These complex conditions often arise in the presence of strong shock waves and pressure gradients [7]. However, the capability of commercial and open-source RANS solvers in predicting these complex high-speed flow phenomena has not been fully assessed. Furthermore, the overall error and uncertainty that can be attributed to the solver selection at these complex conditions has not been quantified in the literature.

Additionally, in wall-bounded fluid flows, a thermal boundary condition at the wall is required to well-pose the problem. Usually, the boundary condition at the wall is assumed either to be adiabatic (zero heat flux), or at a constant temperature. This is an acceptable approximation in low-speed aerodynamic simulations where thermal prediction is less important, but it is critical in high-speed flows where aerodynamic heating needs to be predicted accurately. Predicting the turbulent boundary layer profiles at these high-speed conditions is complex because of the highly-coupled nature of the heat transfer at the wall. The aerothermal heating from the fluid raises the temperature of the solid surface, and conversely, the heated surface of the solid heats up the fluid. This coupling phenomenon reduces the thermal gradient at the wall, reducing heat transfer to the solid body, which further reduces the aerothermal heating on the solid body. Thus, an approach to simulate these conditions is to couple the heat transfer at the solid/fluid wall interface by solving both the Navier-Stokes equations for the fluid flow and the energy equation in the solid simultaneously [8]. This concept is known as: conjugate heat transfer (CHT). Presently, there are a few commercial and open-source CFD solver suites like STAR-CCM+ and SU2 that offer CHT support, however, they have not been validated for high-speed compressible turbulent flows.

Furthermore, a real vehicle also sustains heat loads from within its structure, such as the heat generated by the electronics and propulsion system. The superposition of all heat sources means that the thermal management systems represents one of the central design challenges of a high-speed vehicle. Thus, simulating the thermal loading of the high-speed vehicle becomes an integral part in assessing the thermal and aerodynamic performance of the vehicle.

1.1 Scientific Contributions

Currently, many commercial and open-source RANS-based CFD solvers are used for high-speed flow modelling. Many institutional codes with similar capabilities such as the DLR-TAU [9] and CFL3D [10] are available. Although direct, quantitative, and systematic comparisons of the predictive capabilities of various codes are available in open literature, many

of these comparisons focus on some salient aspect of the code (see e.g. [11, 12, 13, 14, 15]), and most focus on low-speed flows. Fewer researchers have benchmarked CFD codes for high-speed flows, except for one recent example by Hoste et al. [16]. An effort in code comparison also results from the Turbulence Model Benchmarking Working Group from the American Institute of Aeronautics and Astronautics (AIAA). Others have proposed a benchmarking framework targeting direct simulation Monte Carlo (DSMC) code comparisons at hypersonic conditions [17]. More recently, Freno et al. [18] proposed a series of code-verification techniques, primarily directed towards non-equilibrium thermodynamics in high-speed flows. Although these works provide valuable insight into the capabilities of CFD solvers, they do not specifically address the challenges in predicting the turbulent boundary layer of these complex flows.

The thermal boundary condition at the fluid-solid interface of wall-bounded flows plays a key role in predicting drag, flow separation, and boundary layer development. These problems have only been studied using pre-specified wall boundary conditions: usually a constant temperature, constant heat flux, or adiabatic (zero heat flux) boundary condition. However, the aerodynamic and thermodynamic effects of internal heating sources, like the propulsion system in an aerospace vehicle encountered in real engineering applications, has not been explored. To systematically approach this problem, it is important to first thoroughly understand the capability of current CFD solvers.

There are three main objectives for this thesis. The first objective is to detail all the implicit assumptions, simplifications, and heuristic arguments made to the Navier-Stokes equations prior to their implementation in a RANS CFD program. Common heuristics used in low speed flows, such as a constant turbulent Prandtl number of 0.9, break down in the complex flow phenomena prevalent in high-supersonic and hypersonic boundary layers. A complete description of all the simplifications and assumptions would help understand the limitations of certain compressible corrections and turbulence models, as well as understand the cause of disparities between simulations and experimental results.

The second objective is to investigate the capabilities of four well-established CFD codes on predicting key characteristics of the turbulent boundary layer under supersonic and hypersonic conditions, and quantify the variation in their predictions. The implementation of turbulence models within various CFD solvers differ in terms of numerical or algorithmic implementation. Many earlier works conducted in this field focus on the turbulence modellings aspects of the codes, which rightly so, remains the most important source of modelling uncertainty for high-speed wall-bounded flows. Although the discrepancies from numerical or algorithmic implementation are of less important than turbulence modelling assumptions, they remain non-negligible but poorly reported in the literature for high-speed flows.

The third objective is to investigate the impact of internal heating inside a generic rocket design on the kinematic and thermodynamics properties of the external flow using CHT analysis in high-speed flows. There is a scarcity of literature on temperature prediction through CHT analysis for high-speed canonical problems. Thermal predictions for high-speed vehicles with realistic flight trajectories for high-speed aerospace vehicles are rare, with the study from Chandra Murty et al. [4] being one of the few tackling the issue.

In summary, this study aims to provide insight on the major problems associated with predicting aerothermal heating in supersonic and hypersonic flows using CFD solvers, and to investigate the impact of internal heating sources on the thermal and aerodynamic loads on aerospace vehicles. The results from this study provides a better understanding of important design parameters useful for the high-level design of high-speed vehicles.

The dissemination of the scientific contributions of this work are:

- Conference proceeding of AIAA SciTech [19]
- Manuscript on the comparison of error quantification of CFD code (Chapter 4) to be submitted to Journal of Thermophysics and Heat Transfer.
- Manuscript on CHT in high-speed boundary layer flows (Chapter 5) to be submitted to Physics of Fluids.

1.2 Organization of the Thesis

This thesis is divided into five chapters, each for one aspect of the scientific contributions of the work. Chapter 2 presents a literature review of aerothermal heating and CHT methodologies. In Chapter 3, the Favre-averaged RANS equations are derived and all the simplifications and assumptions made for the closure of the equations are outlined. Chapter 3 also describes the turbulence modelling equations using the $k-\omega$ SST turbulence model employed in CFD solvers. Chapter 4 presents the validity of current commercial and open-source CFD solvers in high-speed flows and the expected solver variation in high-speed non-adiabatic wall-bounded flows. Chapter 5 uses the findings from Chapter 3 and 4 to further assess commercial and open-source CFD solvers to validate hypersonic CHT test cases. This chapter also describes the effects of internal heating from a generic rocket engine on the external flow. Finally, Chapter 6 presents the conclusions and recommendations.

Chapter 2

High-Speed Flows with Heat-Transfer

2.1 Literature Review

In high-speed turbulent boundary layers, the accuracy of the near wall simulations largely depends on the treatment of the boundary layer near the wall. There are two methods of simulating near-wall turbulence: a low-Reynolds number model (which means resolving the turbulence profiles down to the wall), and a wall-function approach (which broadly includes all other near-wall modelling approximations). The latter is widely used in CFD codes for its fast convergence rate, robustness, and accuracy in many flows [20]. However, most current wall-function approaches fail when the wall is non-adiabatic [21, 22, 2].

2.1.1 RANS Turbulence Modelling

Modelling of high-speed, wall-bounded, turbulent flow rests on many central assumptions. One of the most common assumptions in compressible turbulent boundary layers is derived from Morkovin's hypothesis [23], which states that the mechanics of compressible turbulent flows differ from their incompressible counterpart only through the differences in their mean-flow fluid properties [24]. Several DNS studies have validated Morkovin's hypothesis for supersonic, adiabatic wall flows [25, 26, 22, 27]. However, RANS-based turbulence models fail to accurately capture the flow features induced by non-adiabatic walls with high wall-cooling rates. This is because RANS turbulence models are generally developed for low-speed flows and are then extended to high-speed flow regimes, and some simplifications made in the modelling of turbulent diffusion and turbulent kinetic energy dissipation fail

in limit cases prevalent in non-adiabatic walls in hypersonic flows [28, 29]. They require additional compressibility corrections to account for the differences [30, 31, 2]. Common RANS turbulence models, such as the Spalart-Allmaras, K-epsilon, Shear Stress Transport (SST) model, have been corrected in the past decade to better account for the strong compressibility effects in high-speed flows [30]; however, many of these corrections originate in free-shear flows and must be further modified for boundary-layer flows [32].

2.1.2 High-speed Flow and Non-Adiabatic Walls

As many high-speed flows occur under complex thermodynamic conditions – especially in the hypersonic regime – the walls are often non-adiabatic, where accurate heat transfer modelling is essential. These complex conditions often arise in the presence of strong shock waves and pressure gradients [7]. These demanding and often conflicting modelling requirements need to be assessed to understand and improve near-wall turbulence modelling predictions. Various adiabatic wall validation studies have been conducted for commercial, open-source, and institutional/academic RANS solvers [33, 34, 35, 36, 37]. However, few validation studies have been conducted using non-adiabatic wall cases [38].

Roy and Blottner [32] proposed a battery of canonical test cases, benchmarked against both experimental and direct numerical simulations (DNS), to assess the turbulence models and their compressibility corrections under hypersonic conditions. Duan et al. [39] and Coleman et al. [40] have performed DNS of fully developed supersonic channel flows between cooled isothermal walls at several wall-cooling rates. In their work, they validate Morkovin's hypothesis, the van Driest transformation, and the Strong Reynolds Analogy (SRA) for flows with significant wall-cooling. RANS-based turbulence models, on the other hand, fail to accurately model the flow features induced by non-adiabatic walls with high wall cooling rates, and thus require additional compressibility corrections to account for the differences. However, most of these compressibility corrections only work in specific cases, and they perform poorly when applied more generally [30].

One of the successful examples of RANS compressibility corrections is from Rumsey [30], wherein many common compressibility corrections for the $k-\omega$ turbulence models in hypersonic boundary-layer applications are tested; only Zeman's [31] dilatation-dissipation correction performs reasonably well at high-Mach-number for cold wall conditions. Rumsey also noted that the accuracy of the $k-\omega$ class of models declines at increasing Mach number for cooled walls cases [30]. Rumsey also tested the $k-\omega$ SST turbulence model using NASA's CFL3D RANS solver on supersonic cases with adiabatic and non-adiabatic walls, where he noted that adiabatic cases represented experimental data far better than

non-adiabatic simulations [30]. Zhang et al. [2] also independently confirmed that the implementation of Zeman's [31] dilatation-dissipation correction works well in cooled-wall cases despite a poorer prediction in the near wall region. Shellabarger conducted a study on shock wave boundary layer interactions (SWBLI) on non-adiabatic flat plates and compression ramps by implementing analytical approaches in STAR-CCM+, and concluded that the current models in STAR-CCM+ are capable of recreating the predicted asymptotic trends in non-adiabatic wall scenarios [41].

A critical DNS database in validating solvers, turbulence models, and compressible corrections in hypersonic conditions was recently created by Zhang et al., wherein high-speed zero-pressure-gradient turbulent boundary layers over a flat plate were simulated for a large range of Mach numbers and wall cooling rates [2]. The data is publicly accessible at the NASA Turbulence Modelling Resource website [42]. Some validation studies conducted in this study reference this extensive database.

Recently, Huang et al. [38] utilized Zhang et al.'s DNS database [2] to assess the accuracy of various turbulence modelling assumptions in a flat plate turbulent boundary layer under cooled-wall conditions, and showed that existing turbulence models provide a good skin friction prediction — although the modelling error is more notable in the transverse heat flux prediction compared to direct numerical simulations.

Thus, the applicability of current near-wall turbulence models in high-speed flows with high-wall cooling rates is still questionable. Due to the increasing interest in this particular field, there are likely disparities in the implementation of compressibility corrections for near-wall turbulence models in commercial and open-source RANS solvers, particularly for cooled-walled cases. Although direct, quantitative, and systematic comparisons of the predictive capabilities of various codes are available in the open literature, many of these comparisons focus on some salient aspect of the code (see e.g. [11, 12, 13, 14, 15]) and mostly focus on low-speed flows. Fewer contributions have sought to benchmark CFD codes at high-speed flow conditions; one recent example is by Hoste et al. [16]. Tangentially, code comparison efforts also results from the Turbulence Model Benchmarking Working Group from the American Institute of Aeronautics and Astronautics (AIAA). Others have proposed a benchmarking framework targeting direct simulation Monte Carlo (DSMC) code comparisons at hypersonic conditions [17]. More recently, work by Freno et al. [18] have proposed a series of code-verification techniques, primarily directed towards non-equilibrium thermodynamics in high-speed flows. Although these works provide valuable insight into the capabilities of CFD solvers, they do not specifically address the challenges in turbulent boundary layer predictions for complex flows.

2.1.3 Conjugate Heat Transfer

An approach to simulating the complex thermal interaction between the wall and the boundary layer is to couple the heat transfer at the solid-fluid interface and to simultaneously solve the Navier-Stokes equations for the fluid flow and the energy equation in the solid. Currently, decoupled conjugate heat transfer simulations are often the standard practice in modelling aerothermal heating. Although this presents an adequate approximation, it does not account for the true coupling observed in realistic CHT problems [43], especially when transient effects are important.

However, the computational costs to truly couple the problems is expensive, because of the vastly different timescales in the conductive heat transfer in the solid and the convective heat transfer in the fluid. Thus, Ferrero et al. proposed hybrid models [8] using a "quasi-stationary" state solver for steady flow problems, wherein the heat-conduction solver is allowed to evolve alone at larger time-step until the wall temperature prediction is a specific percent different to the temperature prediction in the previous iteration. After reaching this threshold, both the heat-conduction and fluid solvers are advanced together at the same time-step. This preserves the coupling between the solid and fluid solvers. Meanwhile, it significantly reduces computational times, by taking advantage of the disparate timescales of the solid and fluid domain.

Another novel approach to accelerating CHT problems is super-time-stepping. This approach is prevalent in astrophysics problems and has recently been applied to hypersonic CHT problems. Instead of checking the criterion for CFL stability at the end of each time-step, an overall stability criterion is checked and maintained for N number of steps. This accelerates explicit CHT simulations without a substantial loss of accuracy. However, increasing the time steps between stability checks decreases the accuracy of the simulation — an analogous to unconditionally implicit schemes [44].

Some multi-physics experiments have been conducted in high-speed flows. Ferrero and D'Ambrosio conducted a critical solver experiment [8] and compared an unsteady CHT RANS simulation of axisymmetric double cones at Mach 4.57 with experimental results from the wind tunnel at the DLR in K oln, Germany. The CHT simulation results showed good agreement with the experimental results, but the simulation showed strong dependence on the boundary condition selection. Dechaumphai et al. conducted another critical multi-physics experiment [45], consisting of a fluid-thermal-structural analysis of a Mach 6.47 flow over a cylinder. These experimental studies (as well as other validation studies conducted using these experiments [4, 46]) provide a source of validation for present commercial and open-source solvers.

CHT has been validated for low speed flows using commercial solvers. For example,

Manna and Chakraborty simulated a low speed laminar flow over a flat plate and a turbulent flow between two parallel plates using ANSYS FLUENT [47]. They observed good match between the model and experimentals in terms of temperature and heat transfer coefficients, validating the capability of CHT solvers in low speed flow.

However, the accuracy of commercial and open-source solvers for simulating high-speed flows with CHT remains uncertain. Marineau et al. tested the CHT capability of the GASP code and validated this commercial CFD solver for high-speed boundary layers, showing a good match against experimental values for surface temperature and Stanton number [48]. However, the CHT was only validated for a nozzle flow, and did not validate the effects of aerothermal heating.

Few studies deal with wall temperature predictions with a CHT analysis for high-speed canonical problems. Ferrero et al. conducted a hypersonic CHT analysis for a homogeneous hemisphere and double cone using a self-developed, loosely coupled high-speed CHT solver [8]. Although the solver was successful, it has not been used to study more practical engineering problems. Thermal prediction studies for high-speed vehicles with real-life flight trajectories are fewer. For example, Chandra Murty et al. [4] conducted a CHT analysis of a flight vehicle's nose cone was conducted at Mach 4.59, using both fluid-solid and solid-solid CHT coupling.

Chapter 3

Theory of the RANS Methodology

3.1 Introduction

This chapter provides a systematic evaluation of the assumptions used in the Reynolds-Averaged Navier-Stokes (RANS) solvers in the context of high-speed flows. RANS solvers rely on turbulence modeling assumptions to approximate the turbulent stresses due to the Reynolds or Favre decomposition. In addition to these modelled transport equations, several other approximations are made to the RANS equations to reach the final implementation in commercial and open-source solvers. The validity of some of these simplifications and analogies break down in certain scenarios, for example, hypersonic flows that are characterized by large temperature gradients and shock-boundary layer interactions. The Favre-averaged Navier-Stokes equations are first derived in full to understand all the implicit assumptions in the solvers. This full derivation presents several additional terms that result from the effects of turbulence, compressibility, or a combination of both. Some terms are modelled using simplifications and analogies, and others are just ignored because of their relative insignificance in the physics of the flow.

3.2 Favre-Averaged Navier-Stokes Derivation

The unsteady, conservative form of the Navier-Stokes equations can be written as follows [6, 49],

$$\frac{\partial \rho}{\partial t} + \frac{\partial}{\partial x_j}\left(\rho u_j\right) = 0 \tag{3.1}$$

$$\frac{\partial}{\partial t}\left(\rho u_i\right) + \frac{\partial}{\partial x_j}\left(\rho u_j u_i\right) = -\frac{\partial p}{\partial x_i} + \frac{\partial \tau_{ji}}{\partial x_j} \tag{3.2}$$

$$\frac{\partial}{\partial t}\left(\rho\left(e + \frac{1}{2}u_i u_i\right)\right) + \frac{\partial}{\partial x_j}\left(\rho u_j\left(h + \frac{1}{2}u_i u_i\right)\right) = \frac{\partial}{\partial x_j}\left(u_i \tau_{ij}\right) - \frac{\partial q_j}{\partial x_j} \tag{3.3}$$

$$p = \rho R T \tag{3.4}$$

where Equation (3.1) is the continuity, Equation (3.2) is the momentum, Equation (3.3) is the energy equation, and Equation (3.4) is the equation of state. Equation (3.4) is the ideal gas law because a key assumption at this stage is that the fluid is a calorically perfect gas. Although the ideal gas law can be applied to high-speed flows, the approximation fails when gas disassociation, ionization, or radiation-dominant effects must be considered — usually past Mach 9.

e corresponds to the specific internal energy and $h = e + p/\rho$ is the specific enthalpy. τ_{ij} is the viscous stress tensor given by,

$$\tau_{ij} = 2\mu s_{ij} + \zeta \frac{\partial u_k}{\partial x_k}\delta_{ij} \tag{3.5}$$

where s_{ij} is the strain rate tensor where a key assumption is that the fluid is Newtonian, such that the viscous stress is linearly proportional to the velocity gradient. In the equation, $\zeta = -\frac{2}{3}\mu$, such that the deviatoric stress does not contribute to the mean normal force when written in Einstein notation. This also invokes the Stokes hypothesis, which assumes that the bulk viscosity of a Newtonian fluid is zero. Although this hypothesis is only applicable for a monotomic gas, it works well for all gasses as long as the velocity gradient is small; this is not the case for high Mach number flows and in shock-waves.

Another implication of a calorically perfect fluid is that the specific heat coefficients c_v and c_p are constant. The calorically perfect assumption fails in the hypersonic regimes, where the specific heat capacities vary with the local temperature of the flow. In such a case, a thermally perfect assumption is more appropriate.

The heat flux vector is found using Fourier's law of conduction. Substituting thermal diffusivity $\alpha = \frac{\kappa}{\rho c_p}$ and the definition of the laminar Prandtl Number $Pr_L = \frac{c_p \mu}{\kappa}$, we have:

$$q_j = -\kappa \frac{\partial T}{\partial x_j} = -\frac{\mu}{Pr_L} \frac{\partial h}{\partial x_j} \tag{3.6}$$

Turbulence is introduced into the conservative forms of the equations using a Favre decomposition approach,

$$\phi = \tilde{\phi} + \phi'' \tag{3.7}$$

where

$$\tilde{\phi} = \frac{1}{\overline{\rho}} \lim_{T \to \infty} \int_t^{t+T} \rho\left(X, \tau\right) u_i\left(X, \tau\right) d\tau \tag{3.8}$$

is the mass-weighted average, and $\overline{(\cdot)}$ is a Reynolds-averaged quantity. The following decomposition approach is used [50],

$$u_i = \tilde{u}_i + u_i'' \tag{3.9}$$
$$\rho = \overline{\rho} + \rho' \tag{3.10}$$
$$p = P + p' \tag{3.11}$$
$$h = \tilde{h} + h'' \tag{3.12}$$
$$e = \tilde{e} + e'' \tag{3.13}$$
$$T = \tilde{T} + T'' \tag{3.14}$$
$$q_j = q_{L_j} + q_j' \tag{3.15}$$

This derivation leads to the following Favre-averaged Navier-Stokes equations,

$$\frac{\partial \overline{\rho}}{\partial t} + \frac{\partial}{\partial x_j}\left(\overline{\rho} \tilde{u}_j\right) = 0 \tag{3.16}$$

$$\frac{\partial}{\partial t}\left(\overline{\rho} \tilde{u}_i\right) + \frac{\partial}{\partial x_j}\left(\overline{\rho} \tilde{u}_i \tilde{u}_j\right) = -\frac{\partial P}{\partial x_j} + \frac{\partial}{\partial x_j}\left(\overline{\tau_{ji}} + \overline{\rho u_j'' u_i''}\right) \tag{3.17}$$

$$\frac{\partial}{\partial t}\left(\overline{\rho}\left(\tilde{e} + \frac{1}{2}\left(\tilde{u}_i \tilde{u}_i\right)\right) + \frac{\overline{\rho u_i'' u_i''}}{2}\right) + \frac{\partial}{\partial x_j}\left(\overline{\rho} \tilde{u}_j\left(\tilde{h} + \frac{\tilde{u}_i \tilde{u}_i}{2}\right) + \tilde{u}_j \frac{\overline{\rho u_i'' u_i''}}{2}\right) =$$
$$\frac{\partial}{\partial x_j}\left(-q_{L_j} - \overline{\rho u_j'' h''} + \overline{\tau_{ji} u_i''} - \overline{\rho u_j'' \frac{1}{2} u_i'' u_i''}\right) + \frac{\partial}{\partial x_j}\left(\tilde{u}_i\left(\overline{\tau_{ij}} - \overline{\rho u_i'' u_j''}\right)\right) \tag{3.18}$$

$$P = \overline{\rho} R \tilde{T} \tag{3.19}$$

The resultant Favre decomposed equations introduces several additional terms that have to either be modelled, simplified, or eliminated depending on their relative importance to the physics of the flow. The most important of the new terms are defined as following [50]. The Reynolds-stress is defined as,

$$\overline{\rho}\tau_{ij} = -\overline{\rho u_i'' u_j''} \tag{3.20}$$

the turbulent kinetic energy,

$$\overline{\rho} k = \frac{1}{2}\overline{\rho u_i'' u_i''} \tag{3.21}$$

and the turbulent heat flux,

$$q_{T_j} = \overline{\rho u_j'' h''} \tag{3.22}$$

A new time derivative is introduced by substituting the definition of the turbulent kinetic energy (Equation (3.21)) into Equation (3.18). Thus, another transport equation is derived [50],

$$\frac{\partial}{\partial t}\left(\overline{\rho} k\right) + \frac{\partial}{\partial x_j}\left(\overline{\rho}\tilde{u}_j k\right) = \overline{\rho}\tau_{ij}\frac{\partial \tilde{u}_i}{\partial x_j} - \overline{\rho}\epsilon + \frac{\partial}{\partial x_j}\left(\overline{\tau_{ji} u_i''} - \overline{\rho u_j'' \frac{1}{2} u_i'' u_i''} - \overline{\rho' u_j''}\right) - \overline{u_i''}\frac{\partial P}{\partial x_i} + \overline{p'\frac{\partial u_i''}{\partial x_i}} \tag{3.23}$$

where ϵ is the Favre-averaged dissipation rate,

$$\overline{\rho}\epsilon = \overline{\tau_{ji}\frac{\partial u_i''}{x_j}} \tag{3.24}$$

With these new definitions, the closure approximations are fully discussed in the next section.

3.3 Closure Approximations in RANS codes

A majority of widely used turbulence models use one- or two-equation turbulence models. Additional approximations are made to model the Reynolds stress and the turbulent heat-flux. Each turbulence model uses its own unique method of closing the equations. However, all turbulence models follow a set of general approximations. [50]. A few important approximations are given below.

3.3.1 Boussinesq Approximation

The Boussinesq approximation relates the Reynolds stress tensor to the mean velocity gradient [51]. It is an extension of the shear stress wherein the effects of turbulence can be modelled as a rise in the "effective viscosity" of the fluid [52]. This additional effective viscosity due to turbulence is called the eddy viscosity, μ_T, and the Reynolds stress tensor is calculated using the following relationship, directly extended from the incompressible case,

$$\overline{\rho}\tau_{ij} \equiv \overline{-\rho u_i'' u_j''} = 2\mu_T \left(S_{ij} - \frac{1}{3}\frac{\partial \tilde{u}_k}{\partial x_k} \right) - \frac{2}{3}\overline{\rho} k \delta_{ij} \tag{3.25}$$

where the eddy viscosity μ_T is calculated using a turbulence model (Spalart-Allmaras, $k-w$, SST among others) [50].

3.3.2 Molecular Diffusion and Turbulent Transport

The molecular diffusion and turbulent transport terms in Equation (3.18) are modelled together in a single model. A common approximation used is [53, 50],

$$\overline{\tau_{ji} u_i''} - \overline{\rho u_j'' \frac{1}{2} u_i'' u_i''} \approx \left(\mu + \frac{\mu_T}{\sigma_k} \right) \frac{\partial k}{\partial x_j} \tag{3.26}$$

where σ_k is a model-specific constant. For subsonic cases, these terms are ignored; in high-speed flows, these terms are considered.

3.3.3 Dilatational Dissipation

The dissipation rate of turbulence energy can be split into two components, the solenoidal dissipation and the dilatation dissipation,

$$\overline{\rho}\epsilon = \overline{\rho}\epsilon_d + \overline{\rho}\epsilon_s \tag{3.27}$$

where,

$$\overline{\rho}\epsilon_s = \overline{\nu}\overline{\rho w_i'' w_i''} \tag{3.28}$$

$$\overline{\rho}\epsilon_d = \frac{4}{3}\overline{\nu}\left(\overline{\rho \frac{\partial u_i''}{\partial i} \frac{\partial u_i''}{\partial i}} \right) \tag{3.29}$$

Huang [27] has shown that the dilatational dissipation is small or negligible in wall-bounded flow, and thus compressibility corrections are not necessary. Some have introduced empirical models for correcting the dilatational dissipation for hypersonic regimes, but they do not tackle the physics of the problem, but rather they are simple corrections to the model [54].

3.3.4 Pressure Dilatation

The pressure dilatation term in the turbulent transport equation appears as,

$$\overline{p' \frac{\partial u_i''}{\partial x_i}}$$

It is the diffusion of turbulent energy caused by pressure fluctuations. Wilcox has stated that "So little is known that it is simply ignored" when referring to pressure dilatation. He goes on to mention that "Even less is known for compressible flows" [54]. Although pressure fluctuations have little to no impact on incompressible and low speed flows, the effects of this term may not be negligible in high-speed flows. Sarkar [55] and Zeman [31] have developed models for pressure dilatation, but since they are not entirely derived from compressible flow relations, they have not gained general acceptance. However, Huang has shown that pressure dilatation is small in adiabatic and non-adiabatic supersonic flat-plate cases [27], which gives a better case for ignoring this term.

3.3.5 Pressure Work

The pressure work appears in many forms throughout the derivation. For example $\overline{u_i''} \frac{\partial P}{\partial x_j}$ and $\overline{u_i''} \frac{\partial P}{\partial x_i}$. It is the effect of turbulence on the work done by the fluid's pressure on the boundaries of a given control volume. Although different turbulence models model pressure work differently, they are all empirically derived [56].

3.3.6 Compressibility Corrections

Additional empirical compressibility corrections are introduced into turbulence models to account for the decrease in mixing-layer growth rate with increasing convective Mach numbers. This dependence of the shear layer growth rate on the convective Mach number has been confirmed and compiled for several experimental studies, resulting in the so-called

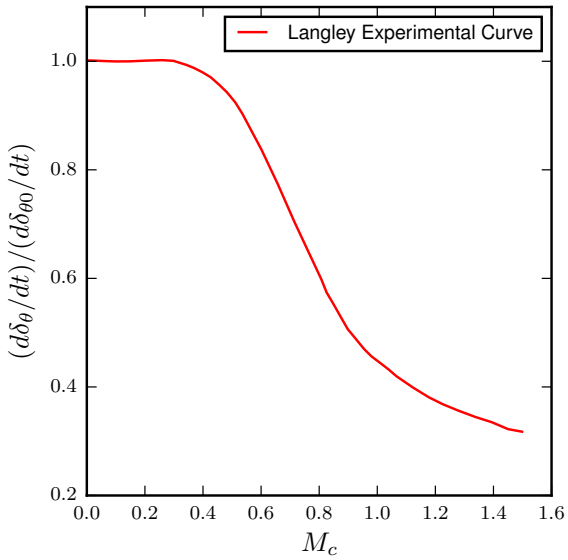

Figure 3.1: Langley experimental curve [1].

Langley experimental curve plotted in Figure 3.1. These additional corrections are treated in a case-by-case basis, depending on the type of turbulence model used [54].

3.3.7 Turbulent Heat Flux

The turbulent Prandtl Number is introduced to approximate the turbulent heat flux vector q_{T_j}. The turbulent Prandtl Number is an extension of the classical Reynolds analogy, and serves to link the turbulent momentum diffusivity to the turbulent thermal diffusivity. There is an assumption made that the turbulent heat flux is proportional to the mean temperature gradient [50, 2],

$$q_{T_j} = \overline{\rho u_j'' h''} = \frac{\mu_T c_p}{Pr_T}\frac{\partial \tilde{T}}{\partial x_j} = \frac{\mu_T}{Pr_T}\frac{\partial \tilde{h}}{\partial x_j}$$

where Pr_T is the turbulent Prandtl number. Equation (3.30) shows that turbulence models like $k-\omega$, $k-\epsilon$, and SST only model the eddy viscosity μ_T. The heat flux is approximated using the turbulent Prandtl number. A common rule of thumb is to use $Pr_T = 0.9$ [57], a value that has been empirically confirmed. However, Wilcox has noted that wall-bounded

heat transfer predictions can be improved by varying Pr_T throughout the boundary layer [50] — a value of $Pr_T = 0.5$ being more appropriate for the outer edge of the boundary layer [50]. The turbulent Prandtl Number extends from Morkovin's hypothesis, and for cases with highly non-adiabatic walls and in flows with high Ma_T, the validity of Morkovin's hypothesis is still not well understood due to the lack of experimental and numerical data available. Thus, the implications of a constant turbulent Prandtl Number is investigated herein in Section 3.5.

3.4 Turbulence and Thermodynamic Modelling

The compressible Favre-averaged Navier-Stokes equations are simplified using the modelling approximations listed in Section 3.3. All the RANS solvers used in this study solve the following equations,

$$\frac{\partial \overline{\rho}}{\partial t} + \frac{\partial \overline{\rho}\tilde{u}_j}{\partial x_j} = 0 \tag{3.30}$$

$$\frac{\partial \overline{\rho}\tilde{u}_i}{\partial t} + \frac{\partial \overline{\rho}\tilde{u}_i\tilde{u}_j}{\partial x_j} = -\frac{\partial \overline{p}}{\partial x_j} + \frac{\partial \overline{\sigma_{ij}}}{\partial x_j} + \frac{\partial \tau_{ij}}{\partial x_j} \tag{3.31}$$

$$\frac{\partial \overline{\rho}\tilde{E}}{\partial t} + \frac{\partial \overline{\rho}\tilde{u}_i\tilde{H}}{\partial x_j} = \frac{\partial}{\partial x_j}\left(\overline{\sigma_{ij}}\tilde{u}_i + \overline{\sigma_{ij}u_i''}\right) - \frac{\partial}{\partial x_j}\left(q_j + c_p\overline{\rho u_j''T''} - \tilde{u}_i\tau_{ij} + \frac{1}{2}\overline{\rho u_i''u_i''u_j''}\right) \tag{3.32}$$

where $\tilde{H} = \tilde{E} + \overline{p}/\overline{\rho}$ is the enthalpy, where $\tilde{E}$ total internal energy which includes the internal energy, kinetic energy, and turbulent kinetic energy. Additionally, $\sigma_{ij} \approx 2\tilde{\mu}\left(\overline{S}_{ij} - \frac{1}{3}\frac{\partial \tilde{u}_k}{\partial x_k}\delta_{ij}\right)$. The overbars, $\overline{f}$, correspond to a Reynolds-averaged quantities, while the tilde, $\tilde{f}$ correspond to the Favre-averaged quantities, $\tilde{f} = \overline{\rho f}/\overline{f}$. The Reynolds fluctuations are denoted by a single prime $f' = f - \overline{f}$ and the Favre fluctuations are denoted by double primes $f'' = f - \tilde{f}$.

In this thesis, the Menter's $k-\omega$ SST model is used to model turbulence in all solvers. It is a two-equation turbulence model that blends the $k-\omega$ and $k-\epsilon$ models [50]. The terms associated with molecular diffusion and turbulent transport are solved by the k and ω transport equations,

$$\frac{\partial \rho k}{\partial t} + \frac{\partial}{\partial x_j}\left[\left(\rho u_j k - \mu + \sigma_k\mu_t\right)\frac{\partial k}{\partial x_j}\right] = P_k - \beta^*\rho k\omega \tag{3.33}$$

$$\frac{\partial \rho \omega}{\partial t} + \frac{\partial}{\partial x_j}\left[\left(\rho u_j \omega\mu + \sigma_\omega\mu_t\right)\frac{\partial \omega}{\partial x_j}\right] = P_\omega - \beta\rho\omega^2 - \rho\sigma_{\omega 2}\frac{1}{\omega}\frac{\partial k}{\partial x_i}\frac{\partial \omega}{\partial x_i} \tag{3.34}$$

where P_k and P_ω are production terms; σ_k and σ_ω are model coefficients. Following a Boussinesq approximation, the Reynolds stress is defined as:

$$\tau_{ij} \equiv \overline{-\rho u_i'' u_j''} = 2\mu_t \left(\tilde{S_{ij}} - \frac{1}{3}\frac{\partial \tilde{u}_k}{\partial x_k} \right) - \frac{2}{3}\overline{\rho} k \delta_{ij} \tag{3.35}$$

where S_{ij} is the mean velocity strain, k is the turbulent kinetic energy, and μ_t is the eddy viscosity computed by the $k-\omega$ SST turbulence model,

$$\mu_t = \frac{\rho a_1 k}{max(a_1\omega, SF_2)} \tag{3.36}$$

where $S = \sqrt{2S_{ij}S_{ij}}$ and F_2 is the second blending function. The denominator of the equation is the shear stress limiter [50].

The quantity $q_j = -\kappa \frac{\partial T}{\partial x_j}$ is the heat flux, where κ is the thermal conductivity and T is the temperature in absolute units. The turbulent heat flux term is modelled based on the Reynolds analogy [53],

$$c_p \overline{\rho u_j'' T''} \approx -\frac{c_p \tilde{\mu_t}}{Pr_t}\frac{\partial \tilde{T}}{\partial x_j} \tag{3.37}$$

where $Pr_t = 0.9$ is the turbulent Prandtl number. The molecular viscosity is modelled based on Sutherlands's law in all the solvers used,

$$\frac{\mu}{\mu_{ref}} = \left(\frac{T}{T_{ref}}\right)^{\frac{3}{2}} \left(\frac{T_{ref}+S}{T+S}\right) \tag{3.38}$$

where $\mu_{ref} = 1.716 \times 10^{-5}$, $T_{ref} = 273K$, and $S_\mu = 111K$ [58].

3.5 Sensitivity of the Turbulent Prandtl Number

The sensitivity of "rule of thumb" quantities must be assessed to understand the implicit assumptions in the derivation of the equations. For example, the turbulent Prandtl Number for air is usually modelled as $Pr_t = 0.9$. This modelling assumption is investigated using a flat plate case, simulated with heated walls in SU2 (an open-source RANS solver [57]), and is compared to DNS measurements by Zhang et al [2]. Zhang [2] has conducted DNS simulations of heated supersonic and hypersonic flat plate boundary layers, and the

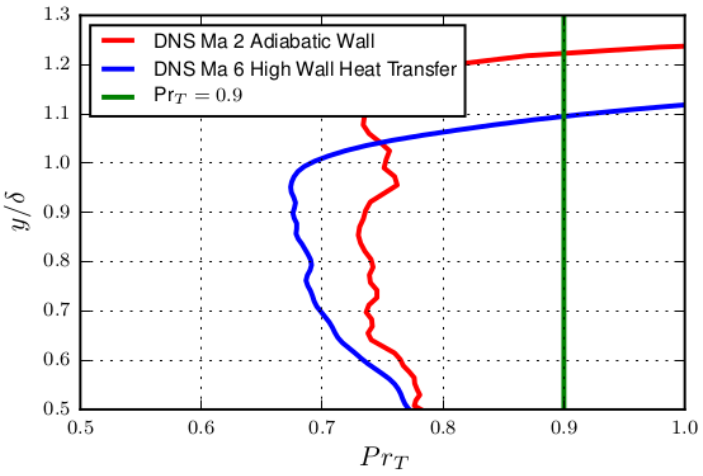

Figure 3.2: Turbulent Prandtl Number variation in DNS results compared to a constant Turbulent Prandtl number assumed in current RANS solvers.

post-processed data for the paper are available online at the NASA Turbulence Modelling Resource website [53].

The turbulent Prandtl numbers for the flows are plotted alongside the constant turbulent Prandtl number assumed in current RANS solvers to note disparities. This is shown in Figure 3.2. The y-values are normalized by the boundary layer thickness δ. The turbulent Prandtl numbers in both the cooled and adiabatic wall cases both show significant departure from $Pr_T = 0.9$. This brings up the question: does the wall-normal temperature profile prediction improve by using an alternate turbulent Prandtl number.

The zero-pressure gradient flat-plate case is described in Figure 3.3, following a similar format as the flat-plate validation cases provided by NASA [53].The SST model is solely used for this study. The boundary and freestream values for the SST turbulence parameters are set based on the recommendations in the original reference [56, 59]. The turbulence inflow conditions are set based on recommendations by Rumsey [53]. More detailed setup description is explained in Section 4.3.1.

Residuals for all RANS cases are converged to a value of 10^{-15}. To compare the boundary layer results from the simulations with the zero-pressure gradient DNS results from Zhang, et al. [2], flow similarity is achieved by attaining a similar momentum thickness

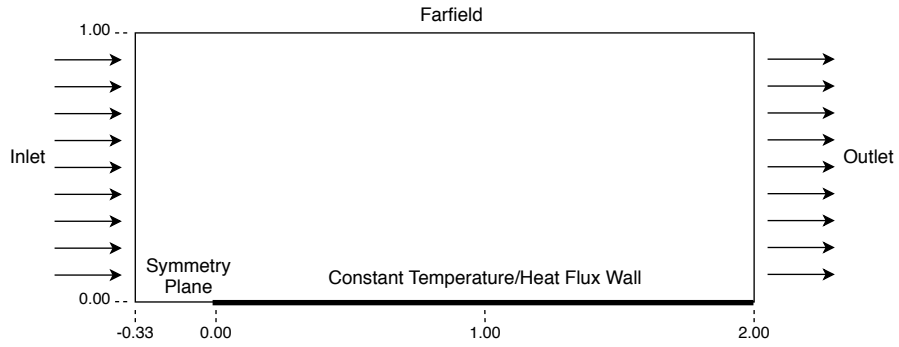

Figure 3.3: Flat plate case description.

Reynolds Number Re_θ, defined as follows,

$$Re_\theta = \frac{\rho_\infty U_\infty \theta}{\mu_\infty}$$
$$\theta = \int_0^\infty \frac{\rho}{\rho_\infty}\frac{u}{U_\infty}\left(1 - \frac{u}{U_\infty}\right) dy$$

which is solved using a Python code. Pr_T values of 0.5, 0.7 and 0.9 are tested for a Mach 2.5 adiabtic wall case and a Mach 6 case with high wall heat transfer ($T_w/T_r = 0.25$). These results are plotted in Figures 3.4 and 3.5. The changes due to varying Pr_T are minimal. However, the decrease of Pr_T increases the error associated with the Mach 2 adiabatic wall case, but conversely qualitatively decreases the error with the Mach 6 high wall heat transfer case. This may be explained due to the empirical nature of $Pr_T = 0.9$. It may potentially work well in cases that are similar to ones used in its derivation, such as the low-supersonic adiabatic case, but the value is not ideal when departing from these conditions. In this case a hypersonic, highly cooled wall case.

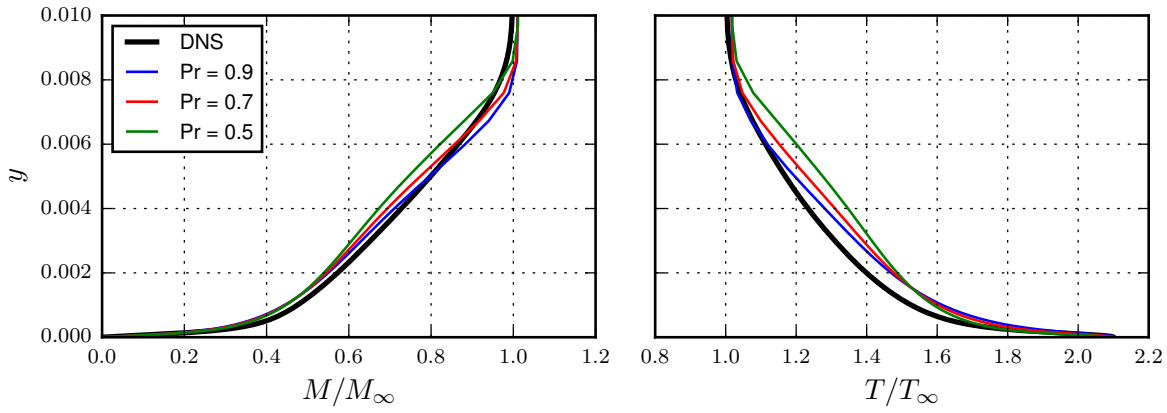

Figure 3.4: Effect of turbulent Prandtl number on the Mach and Temperature profiles at the boundary layer for a Mach 2.5 zero-pressure gradient flat plate case with an adiabatic wall.

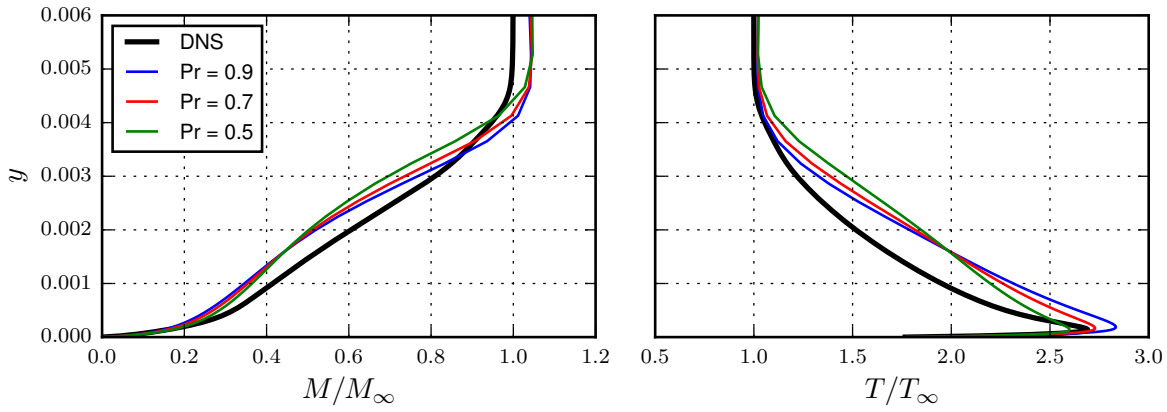

Figure 3.5: Effect of turbulent Prandtl number on the Mach and Temperature profiles at the boundary layer a Mach 5.8 zero-pressure gradient flat plate case with high heat transfer at the wall.

Chapter 4

Error Quantification in CFD Solvers

4.1 Introduction

An optimal CHT simulation is predicated on an accurate estimation of the thermal and velocity gradients at the wall. The state-of-the-art research surrounding models for compressible, wall-bounded turbulent flow still fail in flows characterized by large density fluctuations, shock waves, and high wall heat flux. All of these are flow conditions that a real supersonic or hypersonic vehicle encounters [2]. Since a CHT simulation is run over several additional iterations to couple the fluid solver with the solid conduction solver, any inaccuracy in the fluid solver propagates into the solid solver and produces an inaccurate prediction. This leads into a positive feedback loop of increasing error until convergence. It is thus imperative to understand the errors resulting from the differences in the implementation of a specific turbulence model in CFD solvers.

To reduce the computational requirements, the Navier-Stokes equations are solved under a Reynolds-averaging assumption. The un-closed terms resulting from the Reynolds decomposition are approximated using well-established RANS-based turbulence models. It is the most common approach employed to fluid simulations in engineering. Despite the theoretical importance of the turbulence modeling assumptions, turbulence models used within CFD solvers can differ in terms of numerical or algorithmic implementation. These differences can result in discrepancies in the simulation. These discrepancies are less important than the selection of the turbulence model, but they remain non-negligible and poorly reported for high-speed flows.

Currently, many commercial and open-source RANS-based CFD solvers are used for high-speed flow modeling [60, 61], as well as institutional codes with similar capabilities

such as the DLR-TAU [9] and CFL3D [10]. Although direct, quantitative, and systematic comparisons of the predictive capabilities of various codes are available in the open literature, many of these comparisons focus on some specific aspect of the code (see e.g. [11, 12, 13, 14, 15]) and most focus on low-speed flows. Except for the work by Hoste et al. [16], few have benchmarked CFD codes for supersonic or hypersonic conditions. Some attempted to compare numerical codes as part of the Turbulence Model Benchmarking Working Group from the American Institute of Aeronautics and Astronautics (AIAA) [62, 63]. Others proposed a benchmarking framework targeting direct simulation Monte Carlo (DSMC) code comparisons at hypersonic conditions [17]. More recently, Freno et al. [18] proposed a series of code-verification techniques, primarily for non-equilibrium thermodynamics in high-speed flows. These works provide valuable insight into the capabilities of numerical solvers, but they do not specifically address the challenges in turbulent boundary layer predictions with complex aerothermal heating.

In this section, four well-established CFD codes are assessed based on their overall capabilities for predicting key characteristics of the turbulent boundary layer under supersonic and hypersonic conditions with non-adiabatic walls. The objective is not to establish the superiority of one solver over another, but to quantify the overall error and uncertainty that can be attributed to the solver selection at these complex conditions. Two open-source and two commercial RANS-solvers are compared, all of which use the classical finite volume formulation of the compressible Navier-Stokes equations explained in Chapter 2. The solvers considered are SU2 (open-source), `rhoCentralFoam` part of OpenFOAM (open-source), ANSYS CFX (commercial), and Star-CCM+ (commercial). These codes are used to simulate canonical turbulent boundary layer flows at super- and hypersonic conditions. To facilitate comparison, the cases are simulated using the same turbulence model with identical parameters.

4.2 Turbulent Boundary Layer Considerations

Various solvers are compared in this section, each with many physical and numerical models to choose from. For this reason, certain important definitions and thermodynamic relations are explicitly defined at the onset of this section for tractability. The thermal condition at the wall is controlled in the test cases, which either involves specifying a fixed temperature, or a fixed heat flux boundary condition. For a constant temperature wall condition, the wall temperature is set based on the recovery temperature of the fluid T_r, which is equivalent

to the adiabatic wall temperature T_{aw},

$$T_{aw} = T_r = T_\infty \left(1 + r\frac{\gamma - 1}{2} M_\infty^2\right) \tag{4.1}$$

where T_∞ is the freestream temperature of the fluid, $\gamma = 1.4$ is the specific heat ratio, and r is an empirical factor to account for the imperfect energy recovery. Although the value of r varies with geometry and flow condition, $r = 0.89$ is used to stay consistent with the NASA Turbulence Modelling Resource [53]. The non-dimensional wall temperature is then calculated by normalizing the wall temperature with the recovery temperature $\frac{T_w}{T_r}$, where a value of 1 corresponds to an adiabatic wall, and values above or below unity values represent a heated and cooled wall respectively. The results from the flat plate simulations in this study are compared with the DNS results of Zhang et al. [2]. Flow similarity in the simulation is achieved by attaining a similar momentum thickness Reynolds Number as the DNS cases. This is a post-processed step that is computed using a script in Python using VisIt and MATLAB libraries. RANS simulation results are compared at a certain location downstream of the leading edge where the momentum thickness Reynolds Number Re_θ matches the DNS simulations. Re_θ is defined as,

$$Re_\theta = \frac{\rho_\infty u_\infty \theta}{\mu_\infty} \tag{4.2}$$

where θ is the momentum thickness,

$$\theta = \int_0^\infty \frac{\rho}{\rho_\infty}\frac{u}{u_\infty}\left(1 - \frac{u}{u_\infty}\right) dy \tag{4.3}$$

Three parameters are analyzed on the wall surface in this section, the coefficient of pressure, the skin friction coefficient, and the wall heat flux. Shear stress and heat flux at the wall are computed directly by the RANS solvers to avoid any errors associated with post-processing. These values were manually verified from the result files *a posteriori* to assure consistency. The coefficient of pressure and skin friction are defined as,

$$C_P = \frac{p - p_\infty}{\frac{1}{2}\rho_\infty u_\infty^2} \tag{4.4}$$

$$C_f = \frac{\tau_w}{\frac{1}{2}\rho_\infty u_\infty^2} \tag{4.5}$$

where τ_w is the wall shear stress. The heat flux at the wall is defined as $q_w = -\kappa\left(\frac{\partial T}{\partial y}\right)_{y=0}$, where κ is the thermal conductivity that is calculated using a constant Prandtl assumption

(thus κ varies linearly with viscosity). The non-dimensional heat transfer at the wall is determined using the Stanton number, which is the ratio of the heat transferred to the fluid to the heat capacity of the fluid [64]. The Stanton Number indicates the effectiveness of heat transfer to the fluid,

$$St = \frac{h}{\rho_\infty U_\infty^2 c_p} = \frac{q}{(T_w - T_\infty)\,\rho_\infty u_\infty^2 c_p} \tag{4.6}$$

Alternatively, we can use the wall heat flux coefficient for comparison,

$$C_h = \frac{q_w}{\rho_\infty c_p u_\infty (T_r - T_w)} \tag{4.7}$$

All simulations conducted in this study use air, considered as a calorically perfect gas. The ideal gas law is used as the equation of state in all codes. The calorically perfect assumption breaks down in hypersonic regimes, where the specific heat capacities vary with the local temperature in the flow in addition to the emergence of real gas effects. Thus, a thermally perfect assumption instead of a calorically perfect assumption is more appropriate for these simulations. However, a calorically perfect assumption is explicitly enforced across all the solvers to stay consistent with the DNS simulations conducted by Zhang et al. [2]. The freestream pressure for all the RANS simulations conducted are computed from the ideal gas law.

All solvers in this study use a low-Re modelling approach to resolve the viscous sublayer down to the wall. Menter's $k-\omega$ SST model is used to model turbulence for all solvers, since it is the most widely used turbulence model in high-speed applications [59]. The effects of thermal radiation are not accounted for in the current investigation to stay consistent with the DNS studies [2].

4.3 Summary of Test Cases

Two test cases are systematically studied to assess the predictive capabilities of the four selected solvers. The first case is a supersonic turbulent boundary layer flow over a cooled flat plate; the second case is a supersonic flow over a cold-wall wedge. This section provides an overview of the cases, their geometry, and the type of flows that are simulated. The supersonic flat plate simulations are compared to DNS data, while the results of the supersonic wedge case are compared with each other.

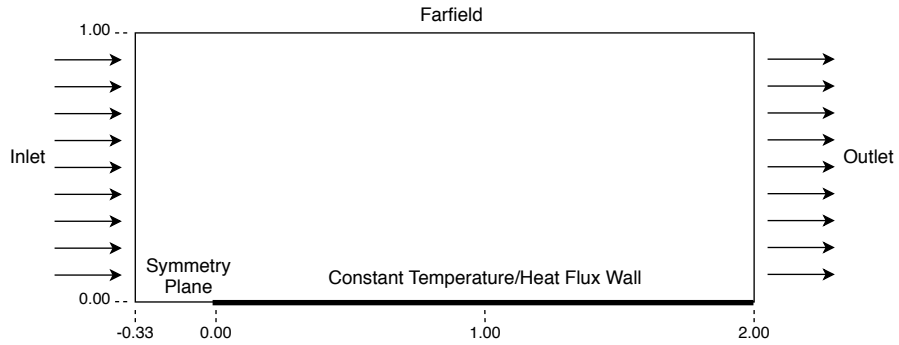

Figure 4.1: Schematic of the flat plate case.

4.3.1 Supersonic Flat Plate

The CFD solvers are compared on a high-speed flow turbulent boundary layer over a cooled wall. Out of simplicity, we consider a zero-pressure gradient, flat plate boundary layer over a fixed temperature cooled wall. A baseline is drawn by comparing the results of the RANS solvers to the DNS results by Zhang et al. [2], whose results are representative of operational conditions of the Mach 6 tunnel at Purdue University, USA. The domain for the RANS simulations consists of a two-dimensional case, where a constant velocity flow enters the inlet. Initially, a slip surface is setup ahead of the non-slip flat plate, allowing the flow to adapt before the emergence of the turbulent boundary layer. The primary dimensions of the computational domain are shown in Figure 4.1, which follows a similar format to the non-adiabatic flat-plate simulations conducted by Rumsey [53].

The length of the flat plate is $L = 2.0$ m to achieve a Reynolds number comparable to the DNS results. This also removes any influence of the outlet boundary on the results in the interior domain of interest. The flat plate begins at $x = 0.0$ and has a lead-in distance of 0.33 m to limit the influence of the inlet boundary condition. These dimensions correspond to a non-dimensional domain size of $Lx = 167\ \delta$ and $Ly = 71.5\ \delta$, with a lead-in of $L_i = 23.6\ \delta$, based on the boundary layer thickness at $x = 1$ m from the leading edge ($\delta = 13.9$ mm).

Table 4.1 summarizes the three condtions simulated. They are: (1) a Mach 2.5 flow over an adiabatic wall ($T_w/T_r = 1$), (2) a Mach 5.86 flow with low/moderate heat transfer at the wall ($T_w/T_r = 0.76$), and (3) a Mach 5.84 flow with high heat transfer at the wall ($T_w/T_r = 0.25$). The heat transfer cases are studied using both a constant wall temperature and heat flux boundary conditions.

Table 4.1: Summary of test cases.

Test Cases	**Freestream conditions**				
	U_∞ (m/s)	T_∞ (K)	ρ_∞	T_w (K)	T_w/T_r
Mach 2.5 - No wall cooling	823.6	270.0	0.10	568.0	1.0
Mach 5.86 - Low wall cooling	870.4	55.0	0.043	300	0.76
Mach 5.84 - High wall cooling	869.1	55.2	0.044	97.5	0.25

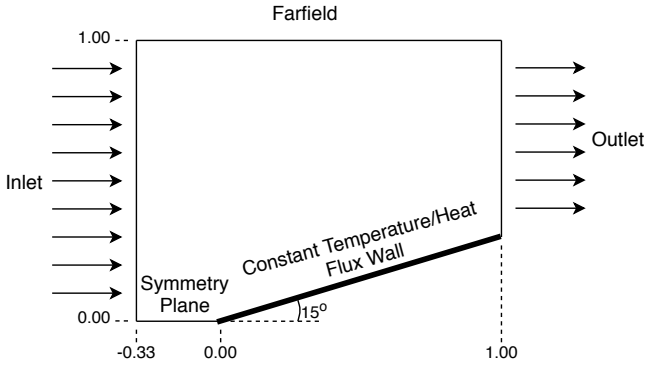

Figure 4.2: Wedge case description.

4.3.2 Supersonic Wedge

A supersonic wedge is considered to study a slightly more complex case with a pressure gradient. The wedge has an angle of $\theta_w = 15\,\text{deg}$. Some numerical studies of supersonic flows over a wedge have been conducted [65, 7], but no DNS simulation nor experimental data is available for the non-adiabatic wall supersonic wedge case [32]. Thus, the results of this test case cannot be assessed against a benchmark simulation. Instead, the variation among the solvers is assessed for the supersonic wedge case. The case configuration is shown in Figure 4.2. Similar to the flat plate boundary layer case, a symmetry (slip) plane is added in front of the non-slip wall to avoid a separation zone at the corner. The analytical solution to the adiabatic supersonic wedge oblique shock angle can be found in the literature [5, 66]. Similar to the flat plate case, three simulations are conducted: (1) a Mach 2.5 flow over an adiabatic wall, (2) a Mach 5 flow with low and (3) high heat transfer at the wall. Both heat transfer cases are simulated with a constant temperature wall.

4.4 Turbulence and Thermodynamic Modelling

The compressible Favre-averaged, Navier-Stokes equations (density-weighted RANS equations) are solved in all the solvers tested in this investigation. See Chapter 2.

The Prandtl number (Pr) is assumed to be constant and set to ~ 0.71 in all solvers, similar to the DNS simulations of Zhang et al. [2]. The fluid is assumed calorically perfect and follows an ideal gas law to relate the pressure, density, and temperature. This assumption is enforced despite its inaccuracy in the hypersonic regimes [5] to stay consistent with the DNS simulations of Zhang et al. [2].

Since the fluid is assumed calorically perfect, the specific heats are independent of temperature (for both constant pressure and volume) and thermodynamically related to the specific heat ratio $\gamma = c_p/c_v = 1.4$ and the universal gas constant $R = c_p - c_v$. The thermal conductivity, κ, is calculated using a constant Prandtl number such that the conductivity varies with viscosity:

$$\kappa = \frac{\mu c_p}{Pr}$$

If a constant Prandtl number cannot be directly specified in the solver (e.g., in Star-CCM+, ANSYS CFX, and `rhoCentralFoam`), the Sutherland's law for thermal conductivity is used instead,

$$\frac{\kappa}{\kappa_{ref}} = \left(\frac{T}{T_{ref}}\right)^{\frac{3}{2}} \left(\frac{T_{ref} + S_\kappa}{T + S_\kappa}\right) \tag{4.8}$$

where $\kappa_{ref} = 0.0241$, $T_{ref} = 273K$, and $S_\kappa = 194K$ [58].

These modelling equations results in flows with Reynolds numbers ranging from $Re = 5 \times 10^6$ to 50×10^6, depending on the test case simulated.

In general, most solvers use freestream conditions to set the initial and boundary conditions of the flow. The isentropic relations are used in cases where stagnation conditions are required instead,

$$\frac{p}{p_t} = \left(1 + \frac{\gamma - 1}{2} M^2\right)^{\frac{-\gamma}{\gamma - 1}} \tag{4.9}$$

$$\frac{T}{T_t} = \left(1 + \frac{\gamma - 1}{2} M^2\right)^{-1} \tag{4.10}$$

where p_t is the total pressure and T_t is the total temperature.

For coomparison, all solvers use Menter's two-equation $k-\omega$ SST for the turbulence modelling, also described in detail in Chapter 2. The turbulence intensity at the inlets is $I = 0.004\%$ and the turbulence to laminar viscosity ratio is $\mu_t/\mu = 0.009$. These values are set based on the supersonic validation test cases conducted by NASA [56], as well as recommendations from Menter's paper[56]. In cases where the turbulence intensity and turbulence kinetic energy cannot be directly enforced, they are converted to their respective turbulence kinetic energy k and turbulence specific dissipate rate ω values using,

$$k = \frac{3}{2}\left(I|u_{ref}|\right)^2 \tag{4.11}$$

$$\omega = \frac{k^{0.5}}{C_\mu^{0.25} L} \tag{4.12}$$

where $C_\mu = 0.09$ is a constant, and L is the reference length scale, in this case, the boundary layer thickness δ.

4.5 Code Descriptions

This investigation compares two open-source and two commercial RANS-based CFD solvers that are based on a classical finite volume formulation of the compressible Navier-Stokes equations. The solvers considered are SU2 (open-source), `rhoCentralFoam` part of OpenFOAM (open-source), ANSYS CFX (commercial), and Star-CCM+ (commercial). These solvers compare a variety of steady-state, transient, pressure-based, and density-based approaches. The numerical schemes for all solvers are chosen to be as consistent as possible. However, this is not true in many cases – for example, due to the lack of implementation of a specific numerical scheme in one of the solvers. In these cases, the code documentation's recommended numerical scheme for supersonic and hypersonic regimes is followed. A brief description of the codes and their respective numerical schemes used in study are detailed below.

SU2

The Stanford University Unstructured (SU2) software is an open-source, density-based RANS solver developed specifically for simulating compressible, turbulent flows in typical aerospace engineering applications [61]. In a density-based solver, the equations for continuity, momentum, and energy are solved, and the pressure is later obtained using an

equation of state. SU2 has been previously used for boundary layer analysis in high-speed flows [16, 67, 68], although a vast majority of scientific studies conducted with SU2 are still limited to low-supersonic conditions. In the present study, the 2-D steady-state simulations are conducted using SU2 $v7.0.3$ "Blackbird".

SU2 solves the compressible, conservative form of the Navier-Stokes equations using a vertex-centered scheme. Several numerical schemes have been implemented in SU2. The SU2 documentation recommends the use of the Roe convection scheme for its superior results in low and moderate supersonic flows, and is thus used in the present study. A Monotonic Upwind Scheme for Conservation Laws (MUSCL) reconstruction is then used to get second order accuracy. Unfortunately, the Roe scheme has been shown to produce non-physical results in hypersonic flows and in the presence of strong shock waves [69]. In these cases, the 2^{nd} order JST scheme is used instead for the hypersonic test cases (Mach ~ 5.8) due to its greater stability in high-speed flows — albeit at a greater computational cost and increased dissipation. In SU2, the turbulent variables are convected using a first-order scalar upwind method, and the viscous fluxes are calculated using the weighted least squares method.

rhoCentralFOAM

Within the OpenFOAM framework, `rhoCentralFoam` is a transient, density-based, compressible RANS code. It has been validated for high-speed inviscid flows [70] and other complex aerospace flows [71]. However, `rhoCentralFoam`'s accuracy in supersonic and hypersonic turbulent boundary layers has yet to be determined. The present study uses the OpenFOAM $v7$ solver suite to run 3-D unsteady simulations for the test cases described in Section 4.3.1.

`rhoCentralFoam` uses a cell-centered approach to solve the unsteady form of the compressible conservative Navier-Stokes equations. The numerical fluxes are solved using a central scheme proposed by Kurganov and Tadmor [72, 73, 74], and a flux limiter function is used to switch between low and high order schemes. Since `rhoCentralFoam` uses a cell-centered approach, a van Leer limiter function is used for the interpolation of all flow variables across a cell face. This has been shown to provide the best balance between performance and solution accuracy [70]. The Gauss linear scheme is used to discretize the gradient and divergence terms of the Navier-Stokes equations, while a corrected version of the Gauss linear scheme is used to discretize the Laplacian term. The local Euler scheme is first used to accelerate the simulation to a pseudo steady-state result, and the Euler implicit scheme is used for time integration.

ANSYS CFX

ANSYS CFX is a fully coupled pressure-based solver created by ANSYS. In a coupled pressure-based solver, the coupled momentum and pressure-corrected continuity equations are solved together, and the energy and turbulence equations are later solved using a decoupled approach. It uses vertex-centered method to solve the compressible conservative form of the Navier-Stokes equations. Several high-speed flows have been simulated successfully using ANSYS CFX in prior studies [75, 76]. In this study, 3-D steady-state simulations are conducted using ANSYS version 2019 R3 [77].

ANSYS CFX uses a high-order advection scheme that automatically blends from a second order to a first order scheme in the presence of shocks [77]. The total enthalphy form of the energy equation (Equation 3.32 is solved by selecting the `Total Energy` model in the solver. This option also includes the contribution of viscous work terms. Since CFX is a pressure-based solver, the `High-Resolution` Rhie Chow algorithm is used for pressure interpolation. The turbulent equations are solved using a first-order upwind method, and the high-speed compressible wall heat transfer model is enabled.

A few additional parameters are also enabled to help with turbulent energy convergence, as recommended by the solver documentation for high-speed flows [77]. The expert parameter `tefnumerics` is set to a value of 1, and `maxcontinuityloops` is set to a value of 2. `Compressibility Control` with the `High-Speed Numerics` options is also enabled, as per the recommendation in the CFX user guide for the SST turbulence model for convergence in regions of very high gradients [77].

Star-CCM+

Star-CCM+ is a commercially available multiphysics code made by the Siemens Product Lifecycle Management Software Inc. and is widely used in the aerospace community [60]. More particularly, it has been used in several supersonic and hypersonic flow studies [41, 78, 79]. Herein, 2-D steady-state simulations are conducted using Star-CCM+ version 2020.2.

Star-CCM+ uses a density-based solver to solve the compressible, conservative form of the Navier Stokes equation with a cell-centered approach. Several numerical schemes are available in Star-CCM+. In this study, the Liou's second order AUSM+ flux vector splitting scheme, recommended by Star-CCM+ for cases of high Mach number [60], is used to calculate the numerical fluxes. The Bi-Conjugate Gradient method is used to solve the system of linear equations, and the gradient model used in this study is the Hybrid

Gauss Least Squares approach. Third-order accuracy is then achieved using MUSCL reconstruction when permissible, since convergence issues and non-physical oscillations are experienced for the hypersonic test cases using a third-order accurate scheme.

Unlike the other solvers, Star-CCM+ also allows the use of certain compressibility correction models to potentially improve the accuracy of the simulation. However, most compressibility corrections are empirically derived, and thus perform poorly when applied in a general context [30]. In this study, the applicability of Sarkar's dilatational dissipation compressibility correction [55] in highly non-adiabatic flows is explored. With Sarkar's compressibility correction enabled, the coefficients β and β^* in Equation (3.33) are replaced by β_{comp} and β^*_{comp},

$$\beta_{comp} = \beta - \beta^* \zeta^* F(M_t) \tag{4.13}$$

$$\beta^*_{comp} = \beta^* \left[1 + \zeta^* F(M_t)\right] \tag{4.14}$$

where ζ^* is a model coefficient, and $F(M_t) = max\left(0, M_t^2 - \left(\frac{1}{4}\right)^2\right)$ is the compressibility function, based on the turbulent Mach number M_t [60]. All Star-CCM+ simulations are also conducted with Durbin's Realizability constraint enabled, where the eddy viscosity in the $k-\omega$ SST model is instead calculated as,

$$\mu_t = \rho k \, min\left(\frac{1}{max\left(\omega/a_1, (SF_2)/a_1\right)}, \frac{C_T}{\sqrt{3}S}\right) \tag{4.15}$$

where C_T is another model coefficient. This follows from the recommendations by the Star-CCM+ documentation [60].

4.6 Simulation Domain and Meshing

2-D and 3-D structured meshes of the flat plate and wedge configuration are created using Pointwise and OpenFOAM's `blockMesh` utility. A 3-D mesh is used in OpenFOAM and ANSYS CFX simulations due to the solvers' inability to use a truly two-dimensional mesh; in the present 3-D cases, only one cell is used in the z-direction. The mesh is refined at the wall for a $Y^+ < 1$ to use the high-resolution turbulence model of the $k-\omega$ SST model. The maximum Y^+ across all simulations and over all the computational domain is $Y^+ = 0.4$. The cell-to-cell expansion ratio at the bottom of the domain is 1.1201. The mesh is also refined in the x-direction at $x = 0$ m to properly capture the complex flow characteristics at the leading edge of the flat plate and the wedge. The cell-to-cell expansion ratio in the

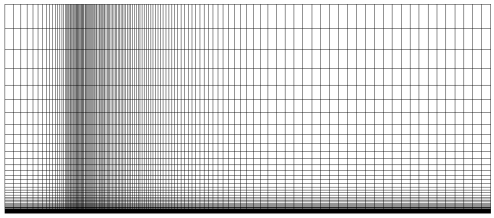

Figure 4.3: Flat plate mesh configuration.

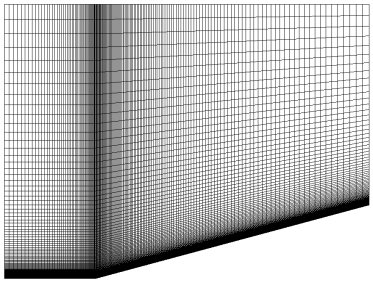

Figure 4.4: Wedge mesh configuration.

streamwise direction at $x = 0.00$ is 1.02234. Figures 4.3 and 4.4 show the meshes used in the flat plate and wedge configuration respectively. A grid dependence study shows good independence of solution from grid sizing and convergence of solution results 4.5.

4.6.1 Boundary Conditions

Every solver has its own "best-practice" for declaring domain boundary conditions for high-speed flows. Table 4.2 shows the boundary conditions used across all the four solver suites. The specific terminology used in each solver is adopted for clarity. For additional information on the implementation of these boundary conditions, the reader should consult the user guides for these codes [80, 77, 81, 60].

4.6.2 Solution Validation

A brief check is conducted to ensure valid solver results. This includs an examination of the convergence behavior and statistics, and the independence of the mesh on the solver results.

Table 4.2: Boundary Conditions Comparison

Solver Suite	**Domain Boundary Conditions**					
	Inlet	**Outlet**	**Symmetry**	**Farfield**	**Wall**	**Front/ Back (3D)**
SU2	Supersonic Inlet	Outlet	Symmetry	Outlet	No-slip	-
OpenFOAM	Fixed Value	Zero Gradient	Symmetry Plane	Zero Gradient	No-slip	Empty
ANSYS CFX	Inlet (Supersonic)	Outlet (Supersonic)	Symmetry	Symmetry	No-slip	Symmetry
Star-CCM+	Freestream	Pressure Outlet	Symmetry	Freesteam	No-slip	-

Convergence

Due to the inherent differences in the algorithmic and physical model, each solver has its own 'best-practice' to maintain stability and achieve steady-state convergence. The classical Courant–Friedrichs–Lewy (CFL) convergence condition needs to be satisfied to maintain numerical stability for explicit time integration schemes. The CFL condition is defined as,

$$Co = \frac{c\,\Delta t}{\Delta x} \leq Co_{\max} \tag{4.16}$$

where c is the speed of sound, Δt is the time step, Δx is the smallest grid element length, and Co is the Courant Number. Although explicit solvers need to stay under the CFL limit of 1, implicit solvers can be accelerated by using a CFL limit much greater than unity because they are unconditionally stable. In Star-CCM+, SU2, and ANSYS CFX, a Courant Number ramp is used to speed up convergence because they are all implicit solvers. The solvers are initially run at a CFL limit of $0.2 - 0.7$ during the first few iteration steps, and later ramping up to a CFL limit of 5, 30, and 100 over thousands of iteration steps.

ANSYS CFX does not allow the definition of an explicit CFL number limit, and instead uses of a local time scale factor for convergence acceleration. CFX simulations are conducted using a local timescale factor of 5 until convergence, and then restart with a physical timescale of $0.0008s$, as recommended in the CFX user guide [77].

Since `rhoCentralFoam` is a transient solver that uses a central scheme, it is thus limited by the $Co \leq 0.5$ condition unique to central schemes [74]. `rhoCentralFoam` simulations

are run using a constant Courant number of $Co = 0.4$.

The convergence of the simulation is assessed in the following three ways:

1. **Numerical Residuals** - The maximum normalized residuals for all three solvers settled below 1×10^{-7} for velocity, temperature, and turbulence quantities. In SU2, the flat plate RMS residuals are below 1×10^{-11}, and in Star-CCM+ and ANSYS CFX, the RMS residuals are below 1×10^{-9}. The RMS residual target for each time-step for OpenFOAM was set as 1×10^{-13}. The time-averaging process for OpenFOAM was conducted over 2000 iteration steps.

2. **Solution Imbalances** - Mass, momentum and energy must be conserved through the simulation domain. The difference between the inlet mass flow and outlet mass flow must be balanced when reaching convergence (similarly for momentum and energy). This is quantified by writing solution imbalances during run-time in the execution windows for all the solvers tested.

3. **Stability of Quantities** - No oscillations are observed with the coefficient of drag, wall heat transfer rate, and coefficient of pressure values while reaching convergence. This was a qualitative assessment, conducted for SU2 by plotting the surface-average quantity history in the post-processing step. Similarly, real-time plotting of the performance parameters were done on ANSYS CFX and Star-CCM+. The stability of performance parameters for OpenFOAM was qualitatively assessed by probing the point of interest in `paraFOAM` and noting the maximum variation between time steps.

Grid Independence

A grid-independence study is conducted to understand the influence of grid size on the result. The coarsity of grids is by calculated using the following relationship,

$$N = 2^n m + 1 \tag{4.17}$$

where N is the number of mesh elements in a given coordinate direction, n is the number of "levels" of mesh refinement, and m is a pre-determined integer that can differ in each coordinate [82]. In this case, $n = 0, 1, 2, 3$ and $m_x = 34$ and $m_y = 24$. Table 4.3 shows the statistics of the meshes used in the grid-independence study. The grid independence checks are conducted on SU2 using a Mach 5 flow, with a constant temperature wall boundary condition set at the recovery temperature of the fluid ($T_w/T_r = 1$).

Table 4.3: Flat Plate Mesh Statistics

Mesh	N_y	N_x	**Total Elements**	**Max.** Y^+
Very Coarse	25	35	875	7
Coarse	49	69	3381	3
Medium	97	137	13,289	0.4
Fine	193	273	52,689	0.2

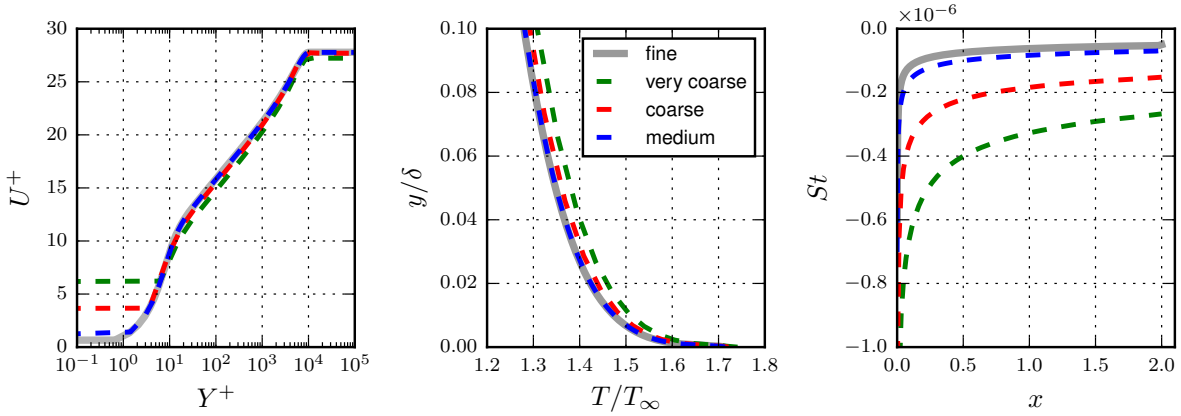

Figure 4.5: Flat plate grid convergence study

Figure 4.5 shows the computed normalized wall-normal velocity and temperature profiles for increasing mesh resolution. Also included is the Stanton number at the constant-temperature wall. The results converge towards the fine mesh. The medium mesh with 135×97 elements is used in the present study, and is considered grid-independent.

4.7 Discussion

This section presents the comparison of the four codes used in this study. The RANS codes are first compared to the mean quantities of equivalent DNS studies. Finally, the codes are compared with each other to quantify the variation between them, for both constant temperature wall and constant wall heat flux conditions.

4.7.1 Solver Accuracy

The commercial and open-source RANS solvers in the study are first assessed on their general ability to accurately capture the boundary layer and wall parameters in high-speed cold-wall flows. A similar study was conducted by Huang et al. [38] in 2019 with greater emphasis on the turbulence model's ability to accurately capture the turbulence statistics near the wall. Conversely, this study emphasizes the error assessment among the solvers to simulate cold-wall, high-speed turbulent boundary layer flows. The wall-normal profiles are extracted at $x = 0.45$ to achieve a similar momentum thickness Reynolds number (Re_θ) as the DNS simulation, and in this case, $Re_\theta = 4845$. Re_θ was calculated in the post-processing step using Equation (4.2).

Figure A1 shows the normalized wall-normal velocity, temperature, and density contours for a Mach 2.5 zero-pressure gradient flat plate case, with no wall cooling. The velocity magnitude, temperature, and density are normalized using freestream values. Overall, all the tested solvers display reasonable agreement with the DNS results. Even in a low-supersonic, no-wall cooling scenario, the wall-normal temperature profile is over-estimated in all codes in the near-wall region ($y/\delta \sim 0.1$). This may be due to an over-prediction of the eddy viscosity very close to the wall, which results in more thermal diffusion through the boundary layer. Figure A4 shows the coefficient of pressure, coefficient of drag, and the Stanton number for the Mach 2 case with no wall cooling. Although a constant wall temperature boundary condition was enforced based on the wall-to-recovery temperature of the fluid $Tw/Taw = 1$, the temperature of the fluid behind the shock wave differs slightly from the freestream temperature of fluid T_∞, resulting in a non-zero heat flux computed at the wall.

Similar agreement is shown in Figure A2 for a Mach 5.86 case with low wall cooling. Note that the effect of an increased Mach number and a slightly non-adiabatic wall has a minor effect on the accuracy of the results. Figure A3 shows the wall-normal profiles for a Mach 5.84 case with a high wall cooling case.

All of the codes deal with the large thermal gradient similarly, and none of them are able to accurately capture the boundary layer. Particularly, the thermal boundary layer is grossly over-estimated throughout the boundary layer; see Figure 4.6. The maximum temperature in the viscous sub-layer, at $y = 0.0002$ ($y/\delta = 0.1$), is also over-predicted by a significant margin. The thermal diffusion in the boundary layer is far greater in the RANS codes as compared to the DNS simulation. The maximum normalized wall distance for the mesh in this simulation is $Y^+ = 0.4$, and further simulations with lower Y^+ values have shown to improve this disparity; however, the impact is only marginal.

Figures A5 and A6 show the wall quantities for the Mach 6 cases with low and high wall

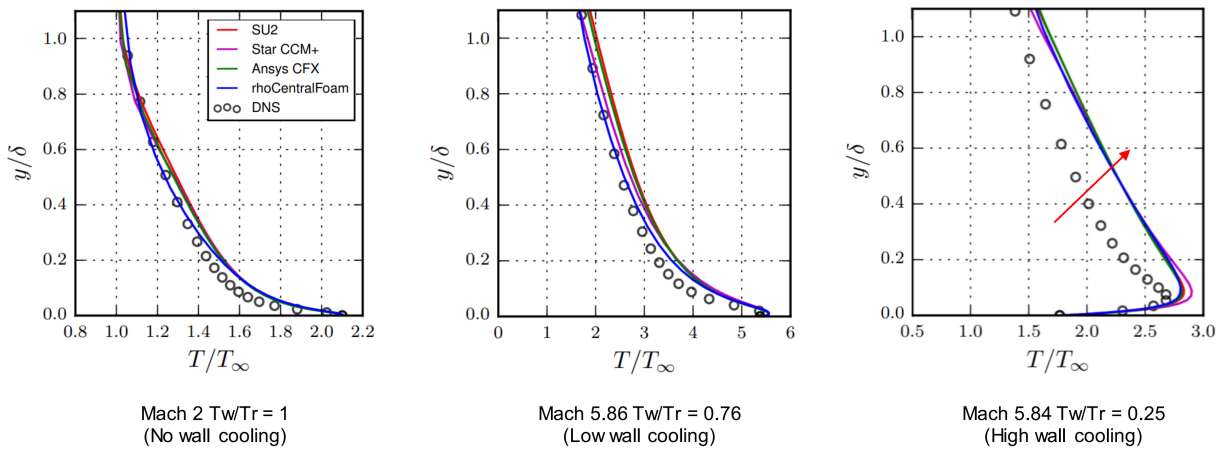

Figure 4.6: Normalized thermal boundary layer for with constant wall temperature boundary condition, compared to DNS simulations of Zhang et al. [2]. The thermal boundary layer is captured less accurately with increasing Mach number, as shown by the red arrow.

cooling respectively. The DNS results for the Stanton numbers are also plotted therein. The Stanton numbers computed for all the solvers tested show similar prediction to the DNS, even in highly non-adiabatic wall cases. This supports similar results obtained by Huang et al [38]. The effect of Sarkar's compressibility correction (a default correction applied by Star-CCM+) is shown in these figures as dotted lines, which shows superior prediction in the wall heat flux in the low-wall cooling case. However, the compressibility correction performs poorly for the highly-cooled wall scenario. This could result from an under-prediction of turbulence dissipation introduced by the limiter function based on the turbulent Mach number; see Equation (4.13) and (4.14).

4.7.2 Solver Comparison

The codes are subsequently compared against each other to quantify the average variation among them. They are also compared in terms of key performance parameters, such as the coefficients of pressure, coefficient of drag, and the heat transfer at the wall. The codes are first compared on a fixed wall temperature case, and then on a case with a fixed wall-heat flux.

Constant Temperature Wall

The difference between the solvers in the boundary layer performance parameters is computed. The wall-normal velocity, density, and temperature profiles are integrated from the bottom wall to 95% of the boundary layer thickness for all solvers. The integrated wall-normal values is averaged among the four solvers. The average and maximum percentage difference between the solvers is computed. The solver variation metrics are computed as follows,

$$Avg.\ Relative = \frac{\sum_{n=1}^{4} \left(\left| \frac{\sum_{n=1}^{4} \bar{F}_n}{4} - \bar{F}_n \right| \right)}{\sum_{n=1}^{4} \bar{F}_i} \times 100\% \tag{4.18}$$

$$Max.\ Absolute = \max \left(\left| \bar{F}_i - \bar{F}_j \right| \right) \qquad i \neq j \tag{4.19}$$

$$Max.\ Relative = \frac{\max \left(\left| \bar{F}_i - \bar{F}_j \right| \right)}{\sum_{n=1}^{4} \bar{F}_n} \times 100\% \qquad i \neq j \tag{4.20}$$

where n represents the solver index (ranging from 1 to 4, since the study compares four solvers), and F is an arbitrary wall-normal property that is numerically integrated through the boundary layer,

$$\bar{F}_n = \int_{y=0}^{y=\delta} F_n(y) dy \tag{4.21}$$

A similar approach is taken for the coefficient of pressure, skin-friction coefficient, and the Stanton number. However, it is integrated along the surface of the wall instead. The effects from the leading edge of the flat plate and the domain outlet are omitted in the solver variation calculations. The omitted regions are displayed as dark grey boxes in Figures A4, A5, and A6. These values are tabulated in Table 4.4 for the constant temperature wall flat plate cases. Note that the numerical values of the maximum absolute variation using this method are only used as a numerical tool to compare absolute values across solvers. Furthermore, the variation calculated using this method is subject to the bounds of integration, i.e. the calculated variation becomes smaller as the integrated length increases.

Figures A1, A2, and A3 shows that the solver variation in the wall-normal velocity, pressure, and density profiles for a constant temperature wall are relatively small, regardless of wall-cooling rates or Mach number. All the solvers tested produce similar results, confirming that the essential physics in the near-wall region of cold-wall supersonic boundary layer flows are adequately captured in all codes. It is noted that pressure-based solvers

(ANSYS CFX) and density-based solvers do not display any significant difference even at these extreme regimes. Particularly, `rhoCentralFoam`, deviates the most from the other solvers in the study. Furthermore, unlike the other codes, `rhoCentralFoam` has little information on solver setup in high-speed flows, and a more optimal simulation setup may produce less deviation.

Variation near the wall in the viscous sublayer is largely more important than variation in the outer region of the boundary layer because most wall values and performance parameters are computed based on the first few grid elements close to the wall. Star-CCM+ displays one such deviation through an over-prediction of temperature in the viscous sublayer for the Mach ∼6 high wall cooling case (Figure A3), which is important to the calculation of the wall heat flux. Key performance parameters such as the coefficient of pressure (C_P), coefficient of skin-friction drag (C_f), and the Stanton Number (St) are plotted along the flat plate wall in Figures A4, A5, and A6 for the Mach 2.5 case, and ∼Mach 6 cases with low wall cooling and high wall cooling cases, respectively. As expected, the performance parameters calculated near the leading edge of the flat plate shows significant variation between the codes, and the variation becomes increasingly apparent with increased Mach numbers. Similar to the wall-normal properties, the pressure and skin-friction coefficient values predicted across the four solvers show relatively little variation for the majority of the plate. The Stanton number, and by extension, the solver-computed heat flux at the wall, qualitatively shows the most variation, shown more clearly in Figure 4.7. The deviation between the Sarkar's compressibility corrected values and the other solver results increases significantly with increased Mach number and wall heat flux.

The variation in the integrated wall-normal profiles and performance parameters for the constant temperature are quantified using Equations (4.18), (4.19), and (4.20) and are tabulated in Table 4.4. Average variation between the solvers is around $2\% - 4\%$. The maximum relative variation between the integrated profiles however is much larger - as much as $\sim 13\%$ for the normalized density profiles. However, the large average and maximum relative variations in the Stanton number for the Mach 2.5 case are artifacts of calculating relative changes close to zero because the heat flux for this test case tends towards zero. A more direct comparison can be attained by comparing the absolute values of these integrated variations, listed in Table 4.4 as "Max. Abs." variations. Although these numbers do not have a physical interpretation, it can be used as an important tool for comparing the variation in the wall-normal profiles for each test case, where the temperature variation in the boundary layer holds the largest absolute variation for all the test cases. This can be partly explained by the integration bounds of the quantification approach (95% of boundary layer thickness) because the Prandtl number for the simulations are 0.71 — meaning the thermal boundary layer is larger than the velocity boundary layer.

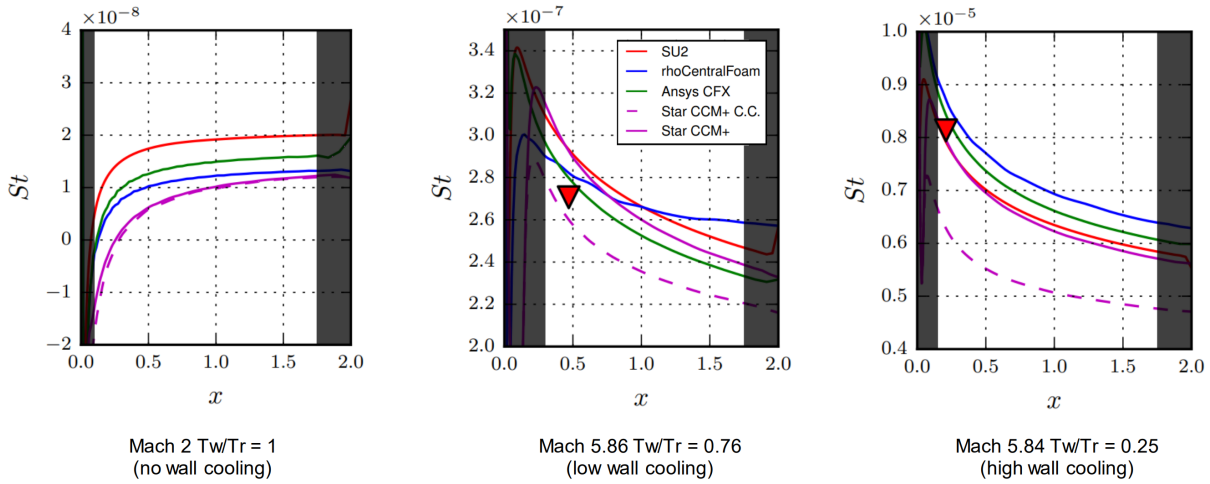

Figure 4.7: Solver comparison of normalized wall heat flux along the surface of the plate. The dotted line is Sarkar's compressibility correction. The red triangle represents DNS simulation results from Zhang et al. [2].

The absolute variation also shows a general trend - an increase in Mach number decreases the solver variation, displayed by a drop in average and maximum variation between the Mach 2.5 and Mach 5.86 simulation, and increasing wall cooling rates increases the maximum absolute variation between the solvers. However, three data points are not enough to confirm this trend, and a deeper investigation is needed to correlate Mach number and non-adiabatic wall effects on solver variation.

Figures B1, B2, and B3 show similar results for the supersonic wedge cases. In these test cases, the flow properties are declared identical to those in the flat plate test cases, and the only difference between them is geometry. The results of `rhoCentralFoam` are omitted from the wedge plots and solver variation calculations because of instabilities and convergence issues, partly due to the lack of available resources to optimally configure a case setup for hypersonic flows. All the solvers are compared at $x = 0.5$ for the wedge case. The average integrated variation in the solvers is similar to the flat plate case, at around 2% to 5% (see Table B1). The supersonic wedge case results show that the maximum variation between the wall-normal profiles is generally reduced when compared to the flat plate cases. On the other hand, the wall quantities like coefficient of pressure, coefficient of skin friction, and wall-heat flux, in general, vary more than their flat plate counterparts. Another interesting observation is that the same trend as in the flat plate case appears here in the wedge case results as well: in general, an increase in Mach number decreases

Table 4.4: Solver variation for a boundary layer on a flat plate with a constant temperature wall.

Prop.	**Mach 2.5** $T_w/T_{aw} = 1$			**Mach 5.86** $T_w/T_{aw} = 0.75$			**Mach 5.84** $T_w/T_{aw} = 0.25$		
	Max. Abs.	**Max. Rel.**	**Avg. Rel.**	**Max. Abs.**	**Max. Rel.**	**Avg. Rel.**	**Max. Abs.**	**Max. Rel.**	**Avg. Rel.**
U/U_∞	4.20e-3	12.64%	3.89%	1.82e-3	13.09%	4.27%	3.27e-3	12.31%	3.36%
ρ/ρ_∞	4.34e-3	13.09%	4.09%	1.34e-3	14.16%	6.76%	3.36e-3	12.51%	3.45%
T/T_∞	4.75e-3	12.75%	4.00%	5.10e-3	10.89%	4.26%	3.45e-3	11.08%	2.90%
c_P	1.28e-2	3.4%	1.15%	2.17e-3	4.06%	1.50%	2.7e-3	5.18%	1.68%
c_f	7.87e-5	2.46%	0.9%	7.98e-5	6.31%	1.73%	1.36e-4	8.21%	2.52%
St	1.67e-8	69.6%	27.00%	2.76e-8	8.73%	2.37%	9.15e-7	11.68%	3.09%

solver variation, and an increasing wall cooling rates increases the variation between the solvers. Once again, these results are not conducive enough to claim a correlation between Mach number and wall cooling effects on solver variation, and a deeper investigation is needed in a later study.

Constant Wall Heat Flux

A complementary study to Section 4.7.2 is conducted with a constant heat flux boundary condition enforced at the wall to observe any notable changes in the variation of the solvers. The physics, model, and numerical definitions are reused from each of the ∼Mach 6 constant temperature wall cases, with the exception of a constant heat flux boundary condition at the wall. Cases for heat flux values of $q_w = -2500\frac{W}{m^2}$ and $q_w = -10,000\frac{W}{m^2}$ are run across all the solvers, for both the flat plate and wedge cases, corresponding to a Stanton number of approximately $St = 3 \times 10^{-7}$ and $St = 7 \times 10^{-6}$ respectively. All the solvers are compared at $x = 0.5$ for both the low and high wall cooling cases. Solution divergence was prevalent in `rhoCentralFoam` when a constant heat flux wall boundary condition was enforced. This is because `rhoCentalFoam` does not have the ability to clip variables when experiencing negative temperatures and densities (common during the first few iteration steps). For this reason, the `rhoCentralFoam` simulation is run using a constant temperature wall condition until convergence, and the simulation is restarted with a constant heat flux boundary condition. However, `rhoCentralFoam` did not converge to a valid result for the $q_w = -10,000W/m^2$ case, and is thus omitted in the plots and solver variation comparison.

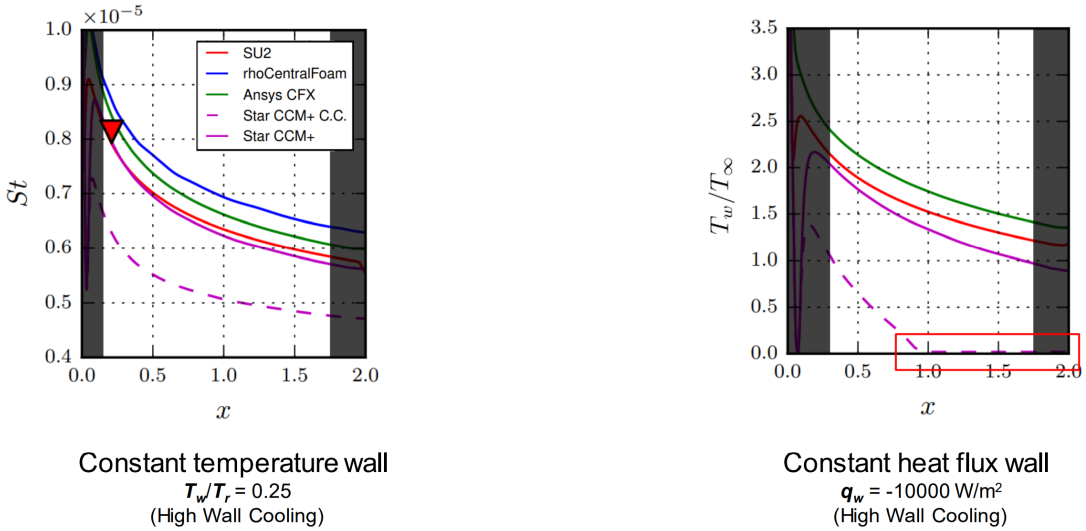

Figure 4.8: Influence of wall boundary condition treatment on solver variation at Mach 6. The dotted line shows Sarkar's compressibility correction failing siginificantly for highly non-adiabatic walls, also producing non-physical values (red box).

Figures C1 and C2 show the normalized wall-normal velocity, temperature, and density profiles for a complementary constant heat flux condition. The thermal and density profile in the viscous sublayer in both these cases vary significantly ($y/\delta \approx 0.01$). This variation is important in real-world engineering cases because minor differences in near-wall flow properties will have a significant impact on the predicted performance parameters. Figures C3 and C4 confirm this, where it is visually apparent that the solver variation using a heat flux boundary condition is greater than the equivalent constant temperature wall cases, particularly with the wall temperature (shown more clearly in Figure 4.8). Similar to the constant temperature wall cases, Sarkar's compressibility correction in Star-CCM+ fails in the $q_w = -10,000 W/m^2$ case and produces non-physical temperatures (see Figure 4.8). This follows the trend that Sarkar's compressibility correction fails progressively for increasingly cooled walls.

Using a similar approach to the previous section, the variation between the solvers for a constant heat flux boundary condition is quantified in Table C1 using Equations 4.20, 4.18, and 4.19. Quantitatively, the solver variation is generally much higher than the Mach $\sim$ 6 constant temperature wall cases for both the wall-normal profiles and wall performance parameters. As noted in the constant temperature wall cases, the solver variation increases with increasingly cooled walls in a constant heat flux boundary condition, shown

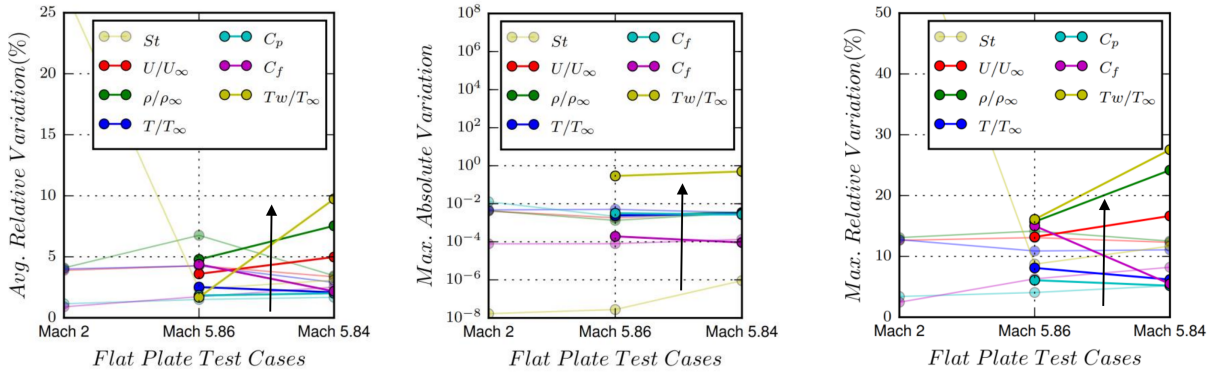

Figure 4.9: A graphical representation of the computed solver variation using Equations (4.18), (4.19) and (4.20). Solver variation generally increases with a constant heat flux wall B.C. as compared to a constant temperature wall B.C.

graphically in Figure 4.9. Particularly, there is a significant variation in wall temperature predictions when compared to other wall quantities, which increases with increased heat flux. The large variation in wall temperatures may arise from the computation and modelling of turbulent heat flux close to the wall. The Boussinesq approximation commonly employed to calculate the mean heat flux $\overline{q}$ has been known to fail near the wall, and RANS solvers typically deal with its near-wall computation uniquely [60]. The variation in the implementation of near-wall turbulent heat flux wall models and blending functions may be the cause for the disparity.

Chapter 5

Internal Heating in Vehicles Using CHT Analysis

5.1 Introduction

High-speed aerospace vehicles experience significant aerodynamic heating in the atmosphere. Simulating the thermal evolution of the aerodynamic surfaces becomes an integral step in developing thermal protection systems for high-speed vehicles. This is also predicated on accurately modelling the turbulent boundary layer.

A boundary condition must be defined at the wall in wall-bounded RANS simulations. Usually, an adiabatic (zero heat flux), constant temperature, or constant heat flux boundary condition is specified at the wall. Consequently, this has also been the approach used in the study thus far. The shortcoming of this approach is that the thermal analysis of the surface cannot be conducted: since the thermal condition of the surface is pre-determined and is user-defined, the resultant wall temperature from aerothermal heating cannot be determined. Furthermore, this approach discounts the highly coupled nature of the problem — the solid surface heats up from aerothermal heating, and the heated solid surface releases some of this heat back into the fluid, affecting the heat transfer rate, and so on. The analysis of aerothermal heating is thus a coupled heat transfer problem, with a solid-fluid interface at the wall, known in literature as a Conjugate Heat Transfer (CHT) problem [8].

In addition to aerothermal heating, the thermal prediction at the surface of a high-speed object will also be affected by the heat loads present within the object. These additional heat loads may present themselves in the form of a heat source like the propulsion system,

or a heat sink like an active cooling design. As detailed in Chapter 4, the inclusion of a highly non-adiabatic wall condition drastically alters the thermal and momentum boundary layer when compared to an adiabatic wall case. It thus becomes crucial to model internal heating and assess its impact on the thermal boundary layer.

This chapter first outlines the basic theory behind CHT analysis and its implementation in CFD codes. Commercial and open-source CFD codes are then validated against experiments to confirm their applicability in high-speed turbulent flows. Finally, the effects of internal heating on the external aerodynamics of a simplistic hypersonic vehicle fuselage are discussed.

5.2 Theory - CHT Analysis

The aim of CHT is to couple two domains – in the context of aerodynamic heating a fluid and solid domain – and estimate the thermal condition at their interface. Two approaches to couple these domains are known in literature as the coupled approach and the conjugate approach.

In the coupled approach, both the solid and fluid energy equations are solved simultaneously. A multi-physics solver solves the Navier Stokes equations in the fluid and the energy equation in solid simultaneously to preserve the coupling at the wall interface. However, this approach presents a huge computational cost because of the added numerical complexity of coupling the domains. Thus, an alternate approach called the Conjugate method is applied to reduce the computational costs.

In the conjugate approach, the fluid and solid solutions are solved independently by two different solvers. The two solutions are later coupled at the interface using a coupling algorithm. The RANS equations are first solved for velocity, pressure, density and temperature in the fluid domain, and the energy equation is solved for temperature in the solid domain. The resultant temperature and heat transfer predictions at the solid–fluid interface are iterated until the predictions from both domains converge to an identical value. At the fluid-solid interface, the heat flux and temperature prediction on either side must be identical. Thus,

$$T_{1|_{\delta_{1-2}}} = T_{2|_{\delta_{2-1}}} \tag{5.1}$$

$$k_1 \frac{\delta T_1}{\delta y}\Big|_{\delta_{1-2}} = k_2 \frac{\delta T_2}{\delta y}\Big|_{\delta_{2-1}} \tag{5.2}$$

where δ is the domain. There are four approaches to couple the two solutions:

1. FFTB (Flux Forward, Temperature Backward)
2. TFFB (Temperature Forward, Flux Backward)
3. hFTB (Heat transfer coefficient Forwards, Temperature Backward)
4. hFFB (Heat transfer coefficient Forwards, Flux Backward)

An appropriate coupling algorithm from the preceding list depends on the type of simulation. The Biot number can provide a reference on the thermal gradient inside the solid from a thermal gradient applied on the surface. The Biot number (Bi) is a dimensionless quantity defined as

$$Bi = \frac{h_f}{\kappa_s} L \tag{5.3}$$

where h_f is the convective heat transfer coefficient, κ_s is the solid thermal conductivity, and L is the characteristic length of the geometry. The approximate heat transfer coefficients for these hypersonic flow simulations can be estimated by running an equivalent constant temperature wall simulation. For example, a Mach 5.86 flat plate case conducted using Standard Sea Level (SSL) conditions, further explained in Section 5.4.1, has an average wall heat flux of approximately $25000 \frac{W}{m^2}$. This gives an average heat transfer coefficient of 2.74×10^6. The characteristic length L is calculated using the ratio of the volume to the surface area,

$$L = \frac{V}{A_{SA}} = \frac{\pi R^2 h}{2\pi R h} = \frac{R}{2} \tag{5.4}$$

For a 150mm diameter sounding rocket fuselage, this value is $0.0375m$. Using the thermal conductivity of 321 stainless steel of 11 $\frac{W}{m^2 K}$,

$$Bi = \frac{(2.74 \times 10^6)(0.0375)}{(11)} >> 1 \tag{5.5}$$

Verstraete and Van den Braembussche are referenced [83] for the correct coupling algorithm selection. They conclude that the temperature forward method (TFFB) must be enforced to obtain convergence if the solid thermal response is more sensitive to a change of the temperature at the solid-fluid interface ($|Bi| >> 1$). They quantify the stability of this method both numerically and algebraically.

For a given time step in the TFFB method, the wall temperature prediction from the fluid solver is used as a known boundary condition (Dirichlet boundary) in the energy equation of the solid solver. The temperature is carried "forward". The heat flux in the solid is solved with the solid energy equation using the wall temperature from the fluid solver as a boundary condition. Similarly, the heat flux prediction from the solid solver is used as a known boundary condition (Neumann boundary) in the fluid solver. The heat flux is carried "backward". This process is iterated during every time step until convergence is achieved.

In unsteady cases, the time step for the numerical simulation with CHT must be selected such that the thermal response within the solid domain does not cross over one computational cell within a prescribed time step,

$$\delta t < \frac{\delta x^2}{2\alpha} \tag{5.6}$$

where δt is the time step, δx is the smallest cell characteristic length in the solid domain, and α is thermal diffusivity of the solid.

5.3 Validation Cases

The validity of commercial and open-source CHT solvers have not been assessed for non-adiabatic hypersonic flows. CHT simulations are conducted using two codes: SU2 and Star-CCM+ — SU2 utilizes the conjugate approach, while Star-CCM+ uses the coupled approach. The extent of previous CHT validation studies conducted on both these solvers are generally limited to low-speed flows in the literature. In this section, a Mach 4.75 with a complex shock-wave boundary layer interaction (SWBLI) is used to validate CHT on Star-CCM+, while a Mach 6 flow over a cylinder is used to validate CHT on SU2.

5.3.1 Mach 4.75 Flow Over an Axisymmetric Double Cone

Star-CCM+ is validated using the experimental results of Francese [3], where an axisymmetric double cone made of Ultra High Temperature Ceramic (UTHC), supported by a copper structure, was tested at Mach 4.75 in the L2K high temperature tunnel [3]. A diagram of the axisymmetric double cone is shown in Figure 5.1.

The free-stream Mach number of the experiment is 4.57, the free-stream pressure is $272Pa$, and the free-stream temperature is $740K$. The test by Francese [3] is performed

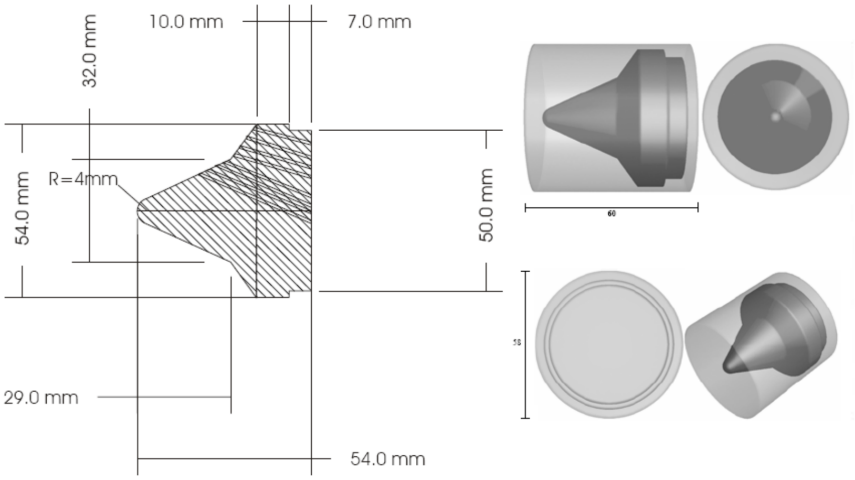

Figure 5.1: Model geometry for the axisymmetric double cone experiment by Francese [3, 4]

with a mixture of Nitrogen and Oxygen as test medium. However, the fluid is assumed to be air as a perfect gas in the Star-CCM+ simulations conducted in this paper. This is a reasonable approximation, since air is composed of 78% Nitrogen and 21% Oxygen [5]. The wall temperature was recorded at two stations: $4mm$ and $35mm$ from the nose for a total time of $90s$. Details on the experiment and measurements can be found in the original reference [3]. CHT validation studies of in-house solvers have been conducted by Ferrero [8] and Chandra Murty [4] using this experiment, and their simulation results also provide a good comparison benchmark for Star-CCM+.

Computational Setup

The mesh used on the Star-CCM+ study contains 140 points in the X direction and 175 points in the Y direction, shown in Figure 5.2. The structured grid is created using PointWise. The mesh is exported in 3-D and is then collapsed into 2-D in Star-CCM+. The mesh is refined at the wall such that $Y+ < 0.15$ throughout the fluid-solid interface to accurately capture the thermal gradient at the wall. The cell-to-cell expansion ratio at the solid-fluid interface is 1.2. The mesh is refined identically in the solid domain and fluid domain.

The boundary conditions used in Star-CCM+ are shown in Figure 5.3. An axisymmetric

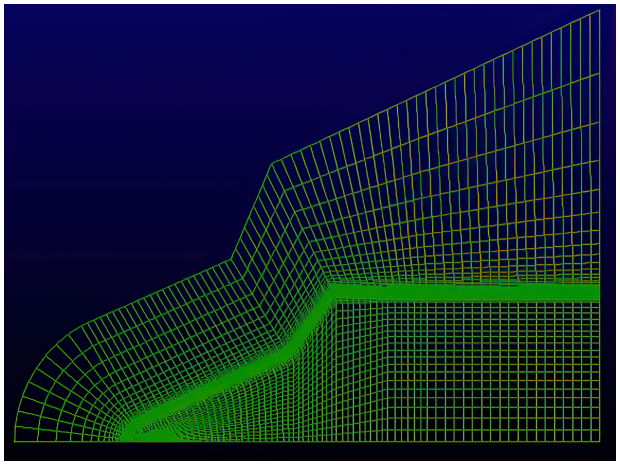

Figure 5.2: Star-CCM+ CHT validation grid.

simulation is conducted using the bottom edge of the domain as the symmetry axis. The simulation setup in Star-CCM+ involves the *Coupled Flow / Energy* model using the density-based solver. Liou's AUSM+ flux vector splitting scheme is used to solve for the inviscid fluxes. The Bi-Conjugate Gradient method is used to solve the system of linear equations, with a Hybrid Gauss Least Squares approach.

A laminar simulation is conducted because the Reynolds number for this flow is approximately 2000. Other validation studies conducted for this experiment also use a similar assumption [4, 8]. Constant material properties are used since the temperature-dependent material properties are not available for UTHC.

The simulation is run using first-order schemes for 200 time steps at a CFL number of 0.1, and is later switched to the Hybrid MUSCL third-order central-differencing scheme. The simulation is run for a total of 60 seconds, with a time-step of $1 \times 10^{-3} s$ for the solid solver. The fluid solver is run using a constant CFL number of 0.5 after the initial 200 time steps.

Results and Discussion

Figure 5.4 shows the temperature evolution of the double cone at 30 seconds. The bow shock at the leading edge of the cone and the separation of the flow is clearly visible. Furthermore, the SWBLI at the secondary ramp is also captured. The solid heats up starting from the leading edge of the cone from aerodynamic heating. Additional aerodynamic heating on the solid is observed at the SWBLI zone on secondary ramp.

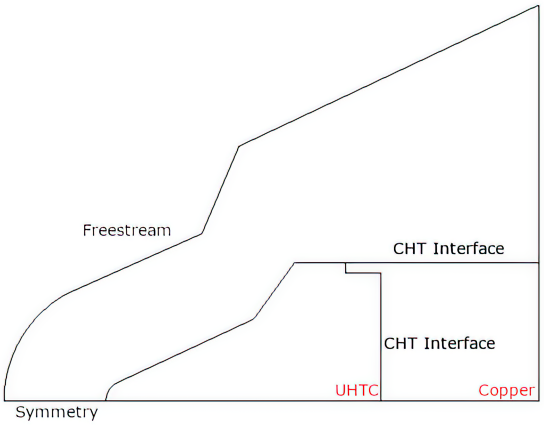

Figure 5.3: Star-CCM+ CHT boundary conditions.

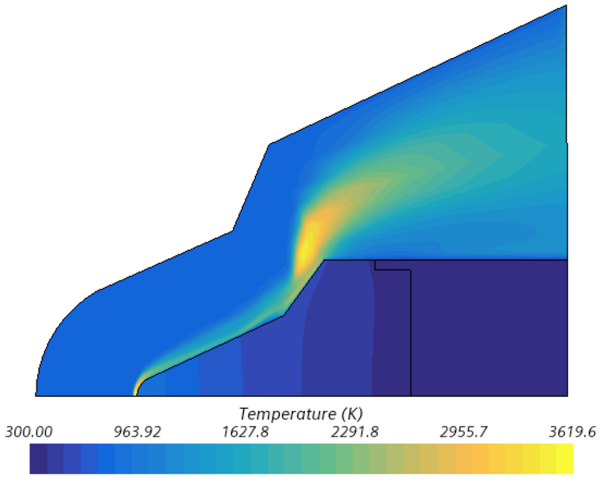

Figure 5.4: Temperature contour of the double wedge after 30 seconds using the Coupled Flow/Energy solver in Star-CCM+.

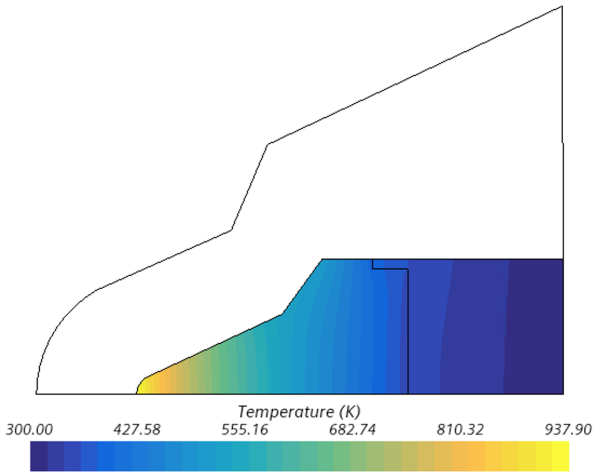

Figure 5.5: Temperature contour of the solid body after 30 seconds using the Coupled Flow/Energy solver in Star-CCM+.

For clarity, Figure 5.5 shows the temperature evolution of only the solid at 30 seconds. The differences in thermal conductivity of the cone (UTHC) and the base mount (copper) is visible. The smaller thermal gradient in the copper, as seen by the thicker gradations in the temperature contour, displays the effect of different thermal diffusivities between the two solid-solid CHT interfaces.

Figure 5.6 shows the simulated temperature histories at $4mm$ and $35mm$ from the nose as compared to experimental values [3] and results from other validation studies [4, 8]. The locations of the two stations are shown in Figure 5.7. Star-CCM+ results generally agree with experimental results and other coupled solvers. The surface temperature prediction at the leading edge ($X = 4mm$) is on par with the constant property results of Chandra Murty et al. [4]. However, the surface temperature prediction deviates significantly with increasing simulation time. This can be due to the coupled nature of the problem: small prediction error over a given time step get carried through the next time step, and the additional coupling iterations in solid and fluid solver further propagates this error.

The bottom set of plots in Figure 5.6 show significant prediction errors in regions of shockwave boundary layer interactions (SWBLIs) at Point 2. The deviation between the simulation and earlier numerical studies [8, 4] is far larger than the deviation at the leading edge. One probable cause is that the assumption of air as a perfect gas may break down at this region. The deviation in these results can also be attributed to lack of mesh resolution in the streamwise direction, and the effects of SWBLIs on the CHT interface may require

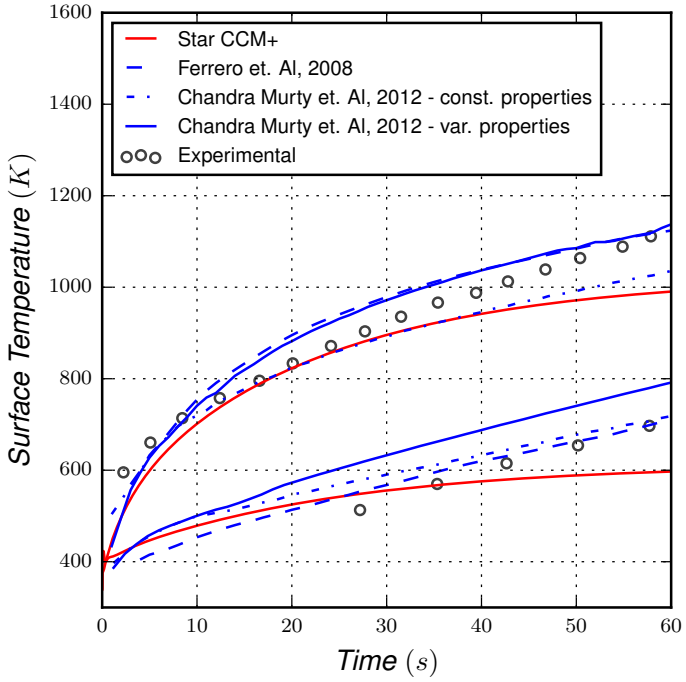

Figure 5.6: Star-CCM+ results for the surface temperature history of the double wedge cone. The upper set of plots show the temperature history at $X = 4mm$ from the nose, and lower set of plots show the temperature history at $X = 35mm$ from the nose.

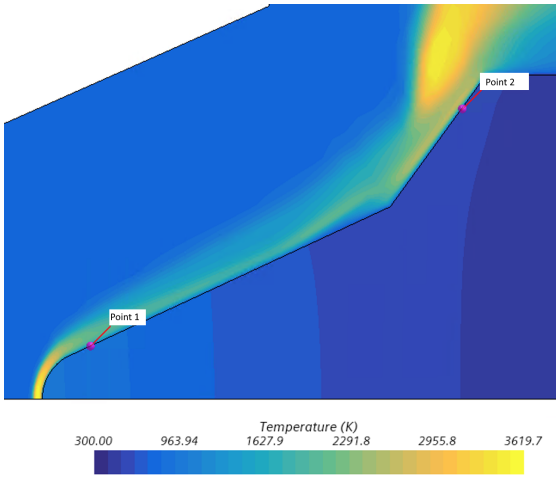

Figure 5.7: Probe locations for the double cone. Point 1 is at $X = 4mm$ and Point 2 is at $X = 35mm$.

further local refinement.

The temperature predictions were found to be highly sensitive to the time step selection in the solid solver. Star-CCM+ uses the fully coupled approach to solve for the interface variables, however, the specifics of the equations are not described in the Siemens PLM documentation [60]. The relaxation of the coupling in a fully coupled solver has been documented by Ferrero and Ambrosio [8], where different temperature histories were predicted based on a 5% and 0.5% threshold. A similar situation may have occurred in Star-CCM+, where a constant relaxation threshold value in the coupling algorithm may be presenting itself as a sensitivity in the ratio of fluid to solid time step $\frac{\Delta t_f}{\Delta t_s}$ selection.

5.3.2 Mach 6 Flow Over a Cylinder

The validation study from Francese [3] cannot be simulated in SU2, since version v7.2.1 Blackbird does not support a CHT analysis for solid-solid interfaces [61]. Instead, an experimental study of a Mach 6.4 flow over a cylinder by Wietling et al. [84] is used for CHT validation on SU2.

Wietling conducted a thermo-structural experimental study of a 321 stainless steel cylinder in cross-flow with a freestream Mach number of 6.47 [84]. The free-stream temperature and pressure are $241.5K$ and $6.47Pa$ respectively. The experiment was conducted in the NASA 8-Foot hypersonic tunnel. The hollow cylinder is $76.2mm$ in diameter and is

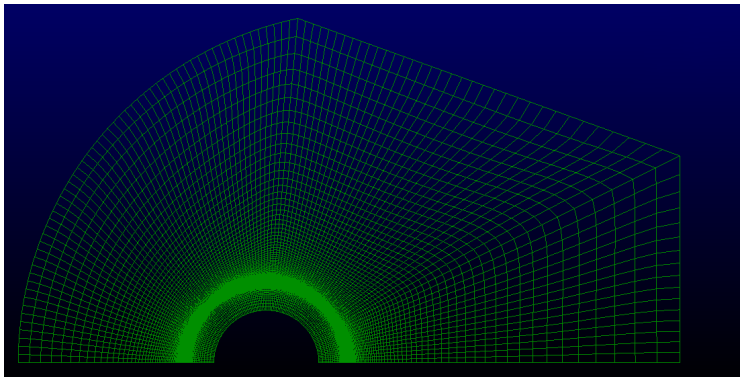

Figure 5.8: SU2 CHT validation grid.

0.5" thick. Details of the experiment and results are given in original reference [84]. The SU2 simulations are also compared with the numerical validation studies [4].

Computational Setup

The mesh contains 65 points in the circumferential direction, and 250 points in the radial direction – 110 of which are in the solid domain (see Figure 5.8). The structured 2-D grid is created using PointWise. Similar to the validation study in Section 5.3.1, the mesh is refined at the wall such that $Y+ < 0.1$ throughout. The cell-to-cell expansion ratio at the bottom of the domain is 1.066. The mesh is refined identically in the solid and fluid domains.

Figure 5.9 shows the boundary conditions used for the validation study. The simulation is conducted using the JST convection scheme with MUSCL reconstruction. Turbulent variables are convected using a first-order scalar upwind method, while the viscous fluxes are calculated using the weighted least squares method. The fluid domain uses a constant Prandtl assumption for thermal conductivity, and varies linearly with viscosity. The experimental setup by Wietling [84] uses the combustion products of Methane as the test gas. However, this study is conducted using air with a perfect gas assumption. The freestream conditions of the experiment result in a Reynolds number of 1.312×10^6, resulting in a laminar to turbulent transition of the boundary layer. For simplicity, a fully turbulent flow assumption is used in the simulation. The simulation is conducted on the upper hemisphere of the hollow cylinder and a symmetry boundary condition is enforced at the bottom of the domain.

SU2 uses an alternate form of the TFFB coupling algorithm, and gives a choice of either

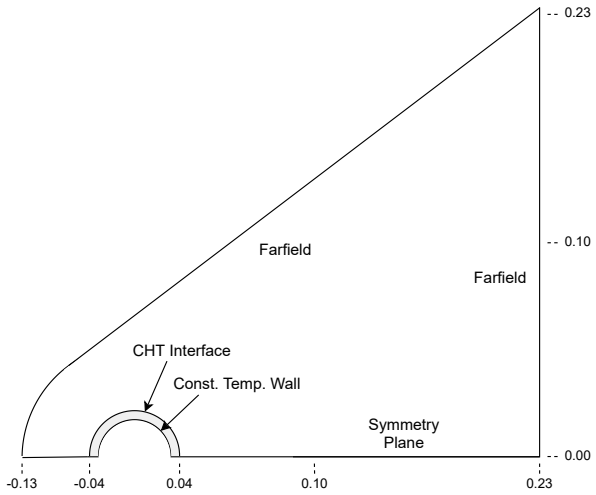

Figure 5.9: SU2 CHT validation boundary conditions.

a Neumann boundary condition or a Robin boundary condition (a weighted Dirchlet and Neumann boundary condition) for coupling the the solid solver to the fluid solver. The *DIRECT TEMPERATURE NEUMANN HEATFLUX* condition is used to stay consistent with the findings of Verstraete and Braembussche [83] (see Section 5.2).

The unsteady simulation is first run with a reduced time-step of $1 \times 10^{-5}s$ until the momentum and mass residuals drop below 1×10^{-3}. The time step is then slowly relaxed to $5 \times 10^{-4}s$, and the simulation is run for 5 seconds of simulation time.

Result and Discussion

Figure 5.10 shows the temperature contour at 5 seconds of simulation time. The bow shock and the stagnation region at the front of the cylinder is well defined. The drop in temperature at the flow separation point is captured well.

Figure 5.11 shows the surface temperature on the cylinder at 5 seconds. SU2 CHT results compares well with both the experimental results [84] and numerical studies [4]. However, the temperature prediction at the stagnation point at the front of the cylinder is significantly underestimated. This could be caused by an incorrect CHT coupling algorithm enforced across a symmetry boundary condition in SU2. Furthermore, the cooling caused by the flow separation is captured well in SU2, and performs on par with the results of Chandra Murty et al [4].

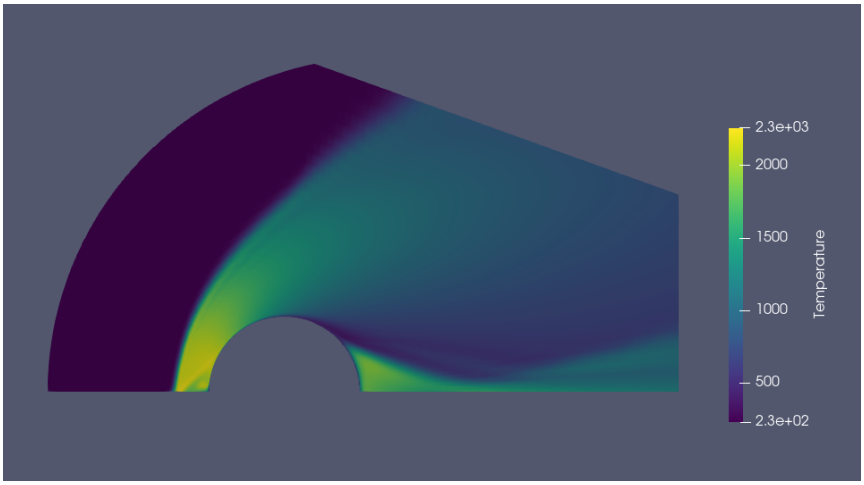

Figure 5.10: Temperature contour of the cylinder validation study after $5s$.

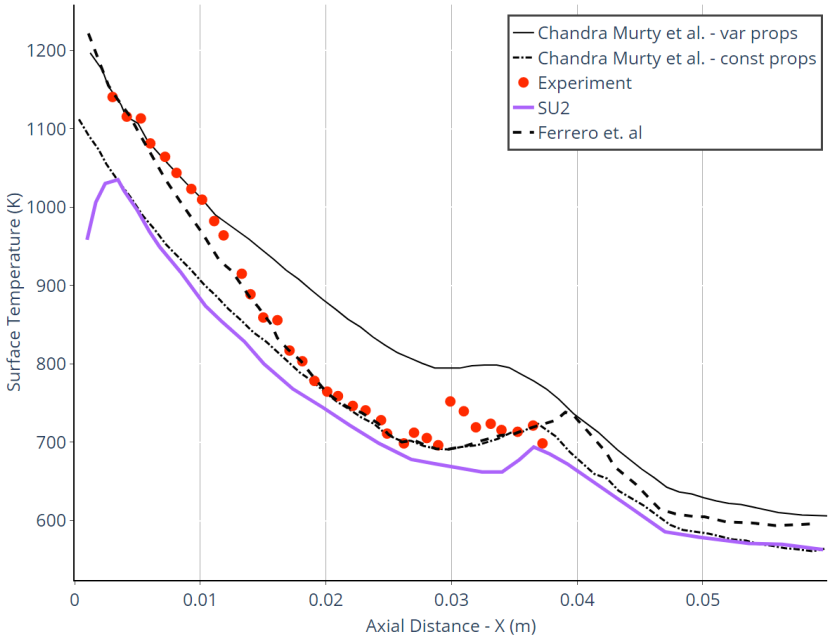

Figure 5.11: Surface temperature after a simulation time of $5s$.

SU2 is used for the internal heating studies conducted in Section 5.4, due to its availability on the supercomputers provided by ComputeCanada. The effects of internal heating in Section 5.4 are analysed far from a leading edge where SU2 performs on par with other numerical solvers. Furthermore, the source code of SU2 is publicly available since it is an open-source RANS solver CHT validation on Star-CCM+ also provides crucial information to the subsequent CHT studies because it validates an axisymmetric flow, unlike the rectilinear flow conducted in the SU2 validation study.

5.4 Internal Heating

High-speed vehicles sustain heat loads from within the vehicle in addition to aerothermal heating in real-world applications. For example, the navigation and guidance modules usually situated at the nose of the rocket produce heat loads in addition to the substantial aerothermal heating. The ability to dissipate the heat generated by these modules must be ascertained. The superposition of all of the heat sources must be modelled to design an efficient thermal management system for the vehicle.

Some points of uncertainty exist because to the lack of literature on the topic. It has been observed numerically and experimentally that the wall temperature has a significant impact on the boundary layer in compressible flows (see Chapter 4). However, the effect of internal heating on the external thermal boundary layer using CHT analysis has not been investigated.

5.4.1 Simulation Setup

Steady-state CHT simulations are conducted on a generic sounding rocket to study the effect of internal heating on the thermal boundary layer. A generic sounding rocket design is shown in Figure 5.12, with a diameter of $250mm$ and a wall thickness of $20mm$.

A boundary condition on the opposite side of the solid domain is required to conduct a CHT analysis. The CHT validation tests conducted in Section 5.3 use a symmetry boundary condition. However, using a constant temperature or constant heat flux boundary condition on the combustion chamber wall provides a great avenue to study the effect of heat sources within the rocket. Since the generic rocket design in Figure 5.12 is highly sensitive to changes in the geometry (for example the design of the nose cone), the problem is simplified further to get a cursory understanding of internal heating effects.

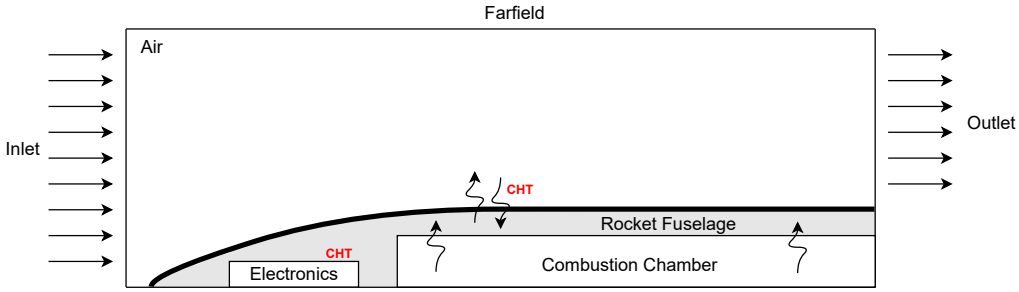

Figure 5.12: Generic rocket case description.

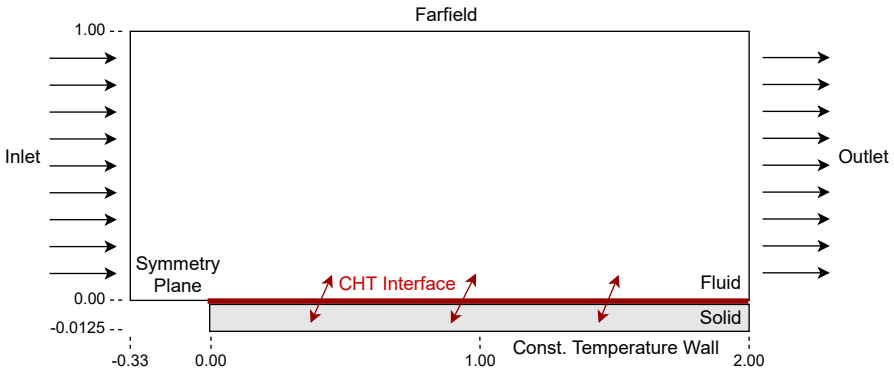

Figure 5.13: Simplified rocket fuselage used for CHT analysis.

The problem is simplified using a flat plate approximation. The effect of this approximation is later analyzed in Section 5.4.4. The combustion chamber temperature is approximated using the adiabatic flame temperature of liquid oxygen and liquid hydrogen, which varies between $3100K - 3650K$ depending on mixture ratio [85]. A combustion chamber wall temperature of $2000K$ is selected to account for imperfect transfer of heat from the combustion gasses to the chamber wall.

Figure 5.13 shows a diagram of the simplified rocket fuselage. Simulations for Mach 2, Mach 5, and Mach 7.5 cases are conducted using Standard Sea Level (SSL) conditions [86]: a freestream pressure, temperature, and density of $101325Pa$, $288.15K$, $1.225\frac{kg}{m^3}$ respectively. An initial solid temperature of $300K$ is selected and the material properties are modelled using 321 Stainless Steel – an alloy used in several aerospace applications.

The SU2 simulation is set up identically to the numerical setup explained in Section

Table 5.1: Comparison of CHT wall temperature predictions using internal heating to recovery temperature estimates.

Case	**CHT** ($300K$ **Chamber Wall**)	**CHT** ($2000K$ **Heating**)	(T_r)
Mach 2.0	386.2K	720.4K	462.2K
Mach 5.0	490.5K	1325.5K	1471.5K
Mach 7.5	790K	1728.9K	2973.4K

5.3.2 to stay consistent with the validation study. Since the test cases are analyzed at steady state, the material and dimensional properties of the solid are inconsequential. The parameters that affect the study are the thermodynamic properties of the fluid, the Mach number of the flow, and the temperature of the inner wall of the solid.

5.4.2 Comparison to Recovery Temperature Estimates

The adiabatic wall temperature is estimated using the recovery temperature of the fluid T_r:

$$T_{aw} = T_r = T_\infty \left(1 + r\frac{\gamma - 1}{2}Ma^2\right)$$

where $r = 0.89$ to account for the imperfect energy transfer at the wall. To understand the applicability of CHT wall temperature estimates, the recovery temperature estimates are compared at Mach 2, Mach 5, and Mach 7.5 using a constant combustion wall temperature of $300K$ and $2000K$. The simulations are conducted using SSL conditions.

Table 5.1 shows the average wall temperature predictions on the plate. As expected, CHT wall-temperature predictions differ significantly to the analytical recovery temperature values T_r because the wall temperature is directly influenced by the constant combustion wall temperature. Using a $300K$ and $2000K$ chamber wall temperature directly influences the heat transfer at the solid-fluid interface by either cooling or heating the wall surface respectively. This converts the CHT analysis to a cold wall or heated wall scenario, and thus accounts for the disparity when compared to an adiabatic wall estimate.

The wall temperature is highly influenced by the proper definition of the chamber wall temperature. An accurate estimation of the combustion chamber wall temperature is necessary to correctly predict the heat transfer at the interface. This may be a simpler problem to solve in real engineering applications when compared to accurately estimating the interface temperature instead.

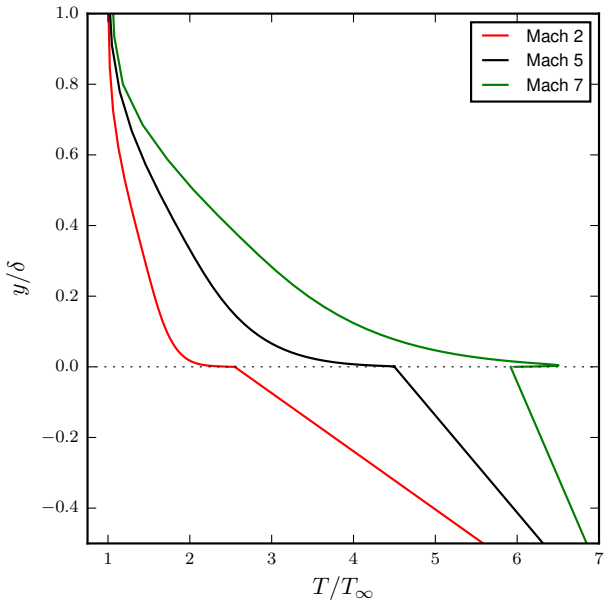

Figure 5.14: Comparison of wall temperature gradients for a CHT analysis with 2000K.

5.4.3 Effect on the Thermal Boundary Layer

Some heat generated in the combustion chamber will be absorbed by the combustion chamber wall, conduct through the fuselage, and will interact with the external flow. The heat produced inside the rocket will affect the external fluid flow, and the effect of internal heating on the thermal boundary layer has to be assessed.

However, wall-normal unit normalization must be discussed prior to comparison. The temperature profiles across the flat plate are usually compared by normalizing the temperature using the free-stream temperature of the fluid (T_∞), and the wall-normal coordinate y is normalized using the thermal boundary layer thickness (δ_T). However, this normalization cannot be applied to the solid domain due to varying boundary layer thicknesses. Instead, the wall-normal coordinate of the solid is normalized using the combustion chamber wall thickness ($20mm$).

Figure 5.14 shows the wall-normal temperature profiles at $0.8m$ downstream of the leading shock. As expected, the thermal gradient in the solid is constant because the simulation is in steady state. However, the thermal interaction at the solid surface shows an interesting feature — an inversion of the wall heat flux vector. When the vehicle is moving

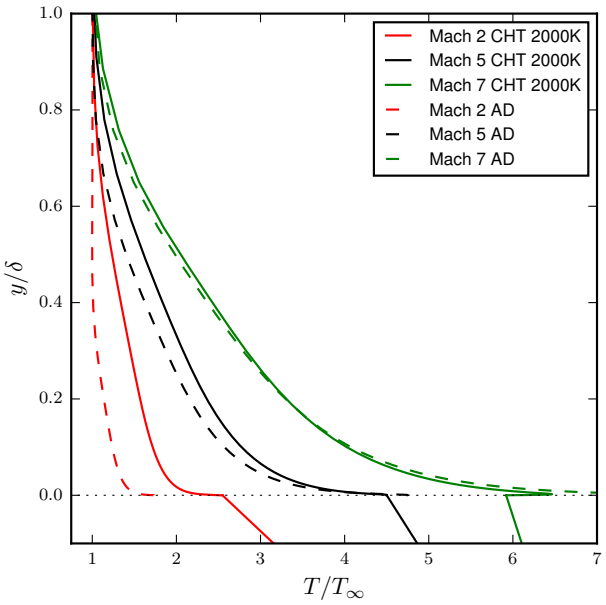

Figure 5.15: Comparison of a flat plate CHT analysis with 2000K internal heating to adiabatic wall scenario.

at low Mach numbers through the atmosphere, the thermal condition at the wall is a cooled wall scenario, since the solid is at a colder temperature than the recovery temperature of the fluid T_r. When heating from the combustion chamber is also included, the interface turns into a heated wall case. However, as the velocity increases, the aerodynamic heating overpowers the internal heating from the combustion chamber, and returns back to a cold wall scenario, where the combustion chamber acts as a heat sink rather than a heat source. This inversion of the heat flux vector is visually observed in Figure 5.14 where the thermal gradient at the wall shows the opposite direction for Mach 7 as compared to Mach 2 and Mach 5 heated wall scenarios.

Figure 5.15 shows the wall-normal temperature profiles from the CHT simulations compared to equivalent RANS simulations with adiabatic walls. The differences in the thermal boundary layer prediction in the log layer reduces significantly with increasing Mach number. The interface (wall) temperature estimate using the adiabatic wall temperature calculation under-predicts in the low Mach number case, and later over-predicts in high Mach Number. In the Mach 2 case, the combustion chamber heating turns the wall into a heated wall, while in the Mach 6 case, the combustion chamber acts as a heat sink and

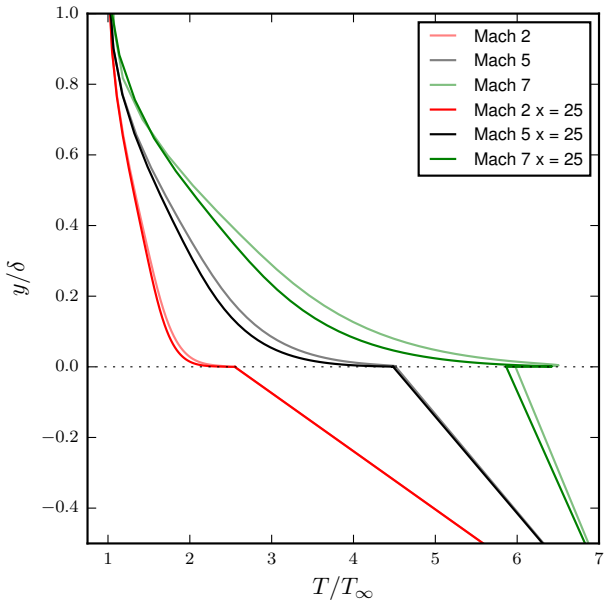

Figure 5.16: Comparison of CHT analysis with 2000K heating at 0.3 m and 2.3m.

cools the interface.

As the Mach number increases and the effect of aerothermal heating increases significantly, the constant temperature combustion chamber wall induces a larger and larger cooling effect at the interface. This results in the viscous sublayer of boundary layer heating up significantly while the interface temperature only increases slightly due to the combustion chamber acting as a heat sink. This is a by-product of the constant temperature combustion chamber wall boundary condition and a steady state CHT analysis. This effect is seen in the wall-normal temperature profile of the Mach 7 CHT simulation in Figure 5.15, and displays recognizable characteristics of a highly cooled wall, similar to the cases simulated in Chapter 4.

Since this is a highly coupled problem, differences in the thermal predictions at the wall will have a potentially large effect downstream of the flow. To quantify the effect of internal heating downstream of the flow, the wall temperature at $X = 0.3m$ and $X = 2.3m$ from the leading edge are compared. Figure 5.16 shows the wall-normal thermal profiles at the two stations for Mach 2, Mach 5, and Mach 7.

Only a minor difference in wall-temperature predictions in both the interface temperature and wall-normal profiles are observed at low Mach number, reaching a maximum

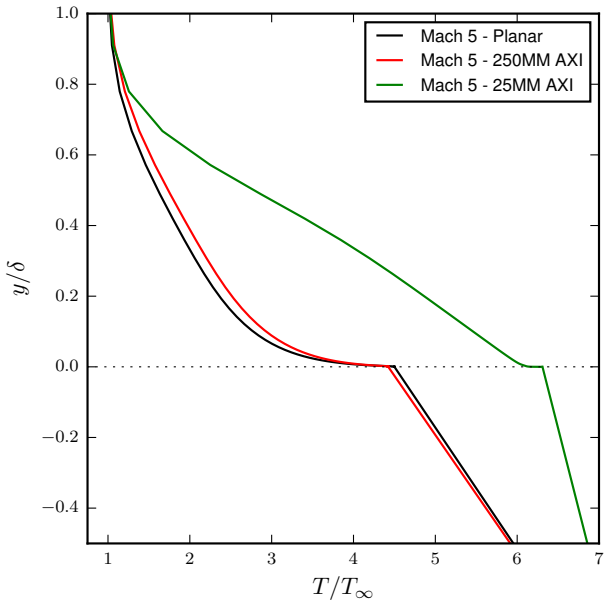

Figure 5.17: Comparison of CHT analysis of a Mach 5 flow with internal heating of 2000K on a planar surface, 250mm cylinder, and a 25mm cylinder.

variation of a few Kelvin. At Mach 7 however the effect is exacerbated, showing significant differences in the wall-normal thermal boundary layer and wall temperature prediction, reaching a wall-temperature variation of $\sim 40K$ between the two stations.

5.4.4 Effect of Axisymmetric Bodies

Most vehicles that travel through the atmosphere have a cylindrical fuselage; for example a rocket or airplane. The simulations conducted thus far use a flat-plate assumption because the diameter of the fuselage is much greater than the boundary layer thickness. The effect of curvature on CHT calculations are two-fold. Firstly, unlike the planar flat plate simulations, the thermal gradient in a cylindrical object is not linear. A lower thermal gradient further from the center is observed because the effective surface area for heat transfer in the cylinder increases with increased distance from the center. Secondly, as the diameter of the axisymmetric body approaches the boundary layer thickness, curvature effects play a significant role in the flow modelling [87]. Simulations identical to ones in Section 5.4.2 are conducted, this time instead as an axisymmetric simulation for diameters

of $25mm$ and $250mm$. The symmetry axis is set at $y = 0$, and the wall-normal temperature profile is compared at $x = 0.8m$ from the leading edge.

Figure 5.17 shows the wall-normal thermal boundary layer for the $250mm$ and $25mm$ axi-symetric simulations compared to the planar simulation. The wall temperature estimates are approximately the same between the planar and $250mm$ axi-symmetric simulations, providing evidence that the flat plate assumption for the $250mm$ rocket is appropriate. The decrease in the wall temperature prediction observed for the $250mm$ axisymmetric simulation is because of the increase in surface area with increasing radius from the heat source.

The $25mm$ axisymmetric simulation on the other hand shows a significantly different thermal boundary layer and wall temperature estimate compared to the planar simulation. An important parameter in axisymmetric wall-bounded flows is the ratio of the boundary layer thickness to the radius of the cylinder [87]. When the cylinder radius approaches the boundary layer thickness, the effects of curvature are significant, and a flat plate approximation fails entirely in predicting the wall-normal and wall properties [87].

A perfect comparison of the wall-normal temperature profiles of a planar and axisymmetric simulation is not possible. The log-law of the wall does not hold for axisymmetric boundary layers [87]. For a potentially better comparison to the planar simulations, the heat flux output of the combustion chamber can be scaled accordingly. For example, since a constant temperature wall is used for the combustion chamber wall, the surface area of the combustion chamber wall can be set equal for an equal heat flux output,

$$A_{s_1} = A_{s_2}$$
$$\frac{r_1}{r_2} = \frac{h_2}{h_1}$$

Chapter 6

Conclusions

This thesis investigates aerothermal heating in high-speed flows from a novel perspective — by studying the impact of internal heat sources on the thermal prediction at the wall using Conjugate Heat Transfer (CHT) coupled to a RANS solver. The predictive modelling of aerothermal heating in high-speed vehicles depends on an accurate modelling of the relevant physics of the problem, particularly within a high-speed turbulent boundary layer. However, the current state-of-the-art research surrounding turbulence models for compressible wall-bounded flows still fail in some specific cases, particularly in flows with large density fluctuations, shock waves, and cases with high wall heat flux. All of these cases are potential flow conditions encountered by supersonic or hypersonic vehicles.

The thesis systematically assesses the capability of current RANS solvers in modelling aerothermal heating. Firstly, the implicit assumptions, simplifications, and heuristic arguments made to the Navier-Stokes equations prior to its implementation in a RANS solver are detailed to understand the cause of disparities between simulations and experimental results. SU2, Star-CCM+, rhoCentralFoam, and Ansys CFX are then validated for supersonic and hypersonic flows with highly non-adiabatic wall cases using DNS results. The approximate error with RANS solvers for the modelling of non-adiabatic high-speed, wall-bounded flows are assessed — an aspect that is poorly reported in the literature in the context of high-speed flows. Next, CHT validation studies are conducted for Star-CCM+ and SU2, using a coupled approach and a conjugate approach respectively, to assess the capability of current commercial and open-source solvers in modelling aerothermal heating using CHT methodologies. Finally, steady-state high-speed CHT simulations on a generic sounding rocket fuselage are conducted to study the effects of internal heating on the external thermal boundary layer.

Results show that the predictions of all RANS codes perform well against the DNS simulations of Zhang et al. [2] in supersonic cases with no wall cooling, but the predictive capabilities is found to decrease with increasing wall cooling rates q_{wall}. Furthermore, the integrated average wall-normal mean property variation in the boundary layer across the RANS codes in a constant temperature wall boundary condition remains relatively low, at approximately $2\% - 4\%$, and the average integrated variation in the coefficient of pressure, skin friction coefficient, and Stanton number is much lower, at approximately $1\% - 3\%$. However, the maximum variation in the integrated profiles are much higher, as much as 13%. The variation between the solvers is found to increase significantly when the flat plate is supplied with a constant heat flux boundary condition as compared to a constant temperature boundary condition, particularly with the thermal prediction at the wall. Wall temperature predictions from the CHT validation studies conducted on Star-CCM+ and SU2 show good agreement with experimental data and other numerical studies. The predicted surface temperatures results match experimental and numerical data accurately, however, notable prediction errors occur in regions of shockwave boundary layer interactions and stagnation points.

The validation tests provide good support for CHT analysis in supersonic and hypersonic boundary layers in open-source and commercial RANS solvers. The methodology is then applied to steady-state high-speed CHT simulations of a generic sounding rocket fuselage at Mach 2, Mach 5, and Mach 7 using Standard Sea Level (SSL) conditions, to study the effect of internal heating of $2000K$ on the external thermal boundary layer. The simulation results show a reversal of the heat flux vector that is observed between Mach 5 and Mach 7, where the case transforms from a heated wall case to a cooled wall case when the Mach number is increased. The Mach number at which the heat flux vector switches direction changes depending on the internal heating rate and the Mach number. By moving the boundary condition from the wall interface to the combustion chamber within the fuselage, the temperature of the combustion chamber wall must be accurately determined instead: a problem which may be simpler to solve than accurately estimating the correct surface temperature.

The results from this thesis provide a better understanding of the capabilities of current RANS solvers in high-speed flows, and important design parameters useful for the high-level design of high-speed vehicles. The studies conducted herein can be further improved and extended. Firstly, the solver variation in non-adiabatic high-speed flows computed in this thesis excludes two important high-speed CFD solvers, CFL3D by NASA [10], and Ansys Fluent [88]. Including the validation results of these solver to the present data will provide a better perspective on the capability of open-source and commercial CFD solvers in non-adiabatic high-speed flows. Trends in the solver variation study show that the solver

variation generally decreases with increasing Mach number, and increases with increasing wall cooling rates. These could be attributed to the differences in the implementation of near-wall turbulence models and boundary conditions (usually derived from adiabatic wall conditions) that become apparent when the wall becomes increasingly non-adiabatic. However, there are too few data points in the current analysis to conclusively ascertain the correlation between Mach number, wall cooling, and solver variation.

The analysis of internal heating on the thermal boundary layer is only limited to steady state CHT in this thesis. Using an unsteady CHT simulation will be the next logical step. Opening up the analysis to an unsteady case presents an opportunity to study other important dimensions of this complex problem; for example, the effect of the material properties of the solid and the wall thickness of the combustion chamber. Furthermore, the vehicle used for CHT analysis flies at a constant altitude at sea-level. The effect of the flight profile and orientation on the aerodynamic heating is significant and an important aspect for future work.

References

[1] H. Foysi and S. Sarkar, "The compressible mixing layer: an LES study," *Theoretical and Computational Fluid Dynamics*, vol. 24, pp. 565–588, 12 2010.

[2] C. Zhang, L. Duan, and M. Choudhari, "Direct numerical simulation database for supersonic and hypersonic turbulent boundary layers," *AIAA Journal*, vol. 56, no. 11, pp. 4297–4311, 2018.

[3] A. Francese, *Numerical and experimental study of UHTC materials for atmospheric re-entry*. Phd. Dissertation, University of Naples Federico II, 2007.

[4] M. S. Chandra Murty, P. Manna, and D. Chakraborty, "Conjugate heat transfer analysis in high speed flows," *Proceedings of the Institution of Mechanical Engineers, Part G: Journal of Aerospace Engineering*, vol. 227, no. 10, pp. 1672–1681, 2013.

[5] J. Anderson, *Modern Compressible Flow: With Historical Perspective*. Aeronautical and Aerospace Engineering Series, McGraw-Hill Education, 2003.

[6] T. B. Gatski and J.-P. Bonnet, "Compressible Flow Dynamics," in *Compressibility, Turbulence and High Speed Flow (Second Edition)* (T. B. Gatski and J.-P. Bonnet, eds.), pp. 23 – 38, Oxford: Academic Press, second edition ed., 2013.

[7] A. Wagner, J. Martinez Schramm, K. Hannemann, R. Whitside, and J.-P. Hickey, "Hypersonic shock wave boundary layer interaction studies on a flat plate at elevated surface temperature," in *22nd International Shock Interaction Symposium*, (Glasgow, UK), pp. 231–243, 03 2018.

[8] P. Ferrero and D. D'Ambrosio, "A numerical method for conjugate heat transfer problems in hypersonic flows," *40th AIAA Thermophysics Conference*, 2008.

[9] K. Hannemann, S. Karl, J. M. Schramm, and J. Steelant, "Methodology of a combined ground based testing and numerical modelling analysis of supersonic combustion flow paths," *Shock Waves*, vol. 20, no. 5, pp. 353–366, 2010.

[10] N. L. R. Center, "CFL3D Version 6 Home Page." https://cfl3d.larc.nasa.gov/. Accessed: 2020-11-09.

[11] S. Haren, *Testing DNS capability of Open FOAM and STAR-CCM+*. Master's thesis, Delft University of Technology, 2011.

[12] M. Winter, "Benchmark and validation of Open Source CFD codes, with focus on compressible and rotating capabilities, for integration on the SimScale platform.," Master's thesis, Chalmers University of Technology, 2014.

[13] F. Greifzu, C. Kratzsch, T. Forgber, F. Lindner, and R. Schwarze, "Assessment of particle-tracking models for dispersed particle-laden flows implemented in OpenFOAM and Ansys Fluent," *Engineering Applications of Computational Fluid Mechanics*, vol. 10, no. 1, pp. 30–43, 2016.

[14] A. Bayon, D. Valero, R. García-Bartual, F. J. Vallés-Morán, and P. A. López-Jiménez, "Performance assessment of OpenFOAM and FLOW-3D in the numerical modeling of a low Reynolds number hydraulic jump," *Environmental Modelling & Software*, vol. 80, pp. 322 – 335, 2016.

[15] Y. Zou, X. Zhao, and Q. Chen, "Comparison of STAR-CCM+ and ANSYS Fluent for simulating indoor airflows," in *Building Simulation*, vol. 11, pp. 165–174, Springer, 2018.

[16] J.-J. O. Hoste, V. Casseau, M. Fossati, I. J. Taylor, and R. Gollan, "Numerical modeling and simulation of supersonic flows in propulsion systems by open-source solvers," in *21st AIAA International Space Planes and Hypersonics Technologies Conference*, (Xiamen, China), AIAA, 2017.

[17] A. O. Ahmad, T. J. Scanlon, and J. M. Reese, "Benchmarking a new, open-source direct simulation monte carlo (dsmc) code for hypersonic flows," in *28th International Symposium on Shock Waves* (K. Kontis, ed.), (Berlin, Heidelberg), pp. 1081–1087, Springer Berlin Heidelberg, 2012.

[18] B. A. Freno, B. R. Carnes, and V. G. Weirs, "Code-verification techniques for hypersonic reacting flows in thermochemical nonequilibrium," *Journal of Computational Physics*, vol. 425, p. 109752, 2021.

[19] I. Syed, J.-P. Hickey, E. Farnfield, and B. Godbolt, "Error quantification among CFD solvers for high-speed, non-adiabatic, wall-bounded turbulent flows," in *AIAA Science and Technology Forum and Exposition*, (Virtual Event), AIAA, 01 2021.

[20] X. Wang, T. J. Craft, and H. Iacovides, "An analytical wall function for 2-D shock wave/turbulent boundary layer interactions," *Proceedings of the World Congress on Mechanical, Chemical, and Material Engineering*, pp. 1–10, 2017.

[21] A. Trettel and J. Larsson, "Mean velocity scaling for compressible wall turbulence with heat transfer," *Physics of Fluids*, vol. 28, no. 2, 2016.

[22] P. G. Huang and G. N. Coleman, "Van driest transformation and compressible wall-bounded flows," *AIAA Journal*, vol. 32, no. 10, pp. 2110–2113, 1994.

[23] M. V. Morkovin, "Effects of compressibility on turbulent flows," *Mécanique de la Turbulence*, p. 367–380, 1962.

[24] A. Smits and J.-P. Dussauge, *Turbulent Shear Layers in Supersonic Flow*. New York, NY: Springer New York, 1 ed., 2006.

[25] L. Duan, I. Beekman, and M. P. Martín, "Direct numerical simulation of hypersonic turbulent boundary layers. Part 3. Effect of Mach number," *Journal of Fluid Mechanics*, vol. 672, pp. 245–267, 4 2011.

[26] Y.-S. Zhang, W.-T. Bi, F. Hussain, and Z.-S. She, "A generalized Reynolds analogy for compressible wall-bounded turbulent flows," *Journal of Fluid Mechanics*, vol. 739, p. 392–420, 2014.

[27] P. G. Huang, G. N. Coleman, and P. Bradshaw, "Compressible turbulent channel flows: DNS results and modelling," *Journal of Fluid Mechanics*, vol. 305, pp. 185–218, August 1995.

[28] H. Tang and Z. Gao, "Investigation of turbulence models with compressibility corrections for hypersonic boundary flows," *Advances in Mechanical Engineering*, vol. 7, no. 12, p. 1687814015620319, 2015.

[29] Z. Zhu, X. Zhang, X. Wang, and L. Zhang, "Analysis of compressibility corrections for turbulence models in hypersonic boundary-layer applications," *Journal of Spacecraft and Rockets*, vol. 57, no. 2, pp. 364–372, 2020.

[30] C. L. Rumsey, "Turbulence models in hypersonic boundary layer applications," Tech. Rep. April, National Aeronautics and Space Administration, Hampton, Virginia, 2009.

[31] O. Zeman, "A new model for super/hypersonic turbulent boundary layers," in *31st Aerospace Sciences Meeting*, AIAA, 1993.

[32] C. J. Roy and F. G. Blottner, "Review and assessment of turbulence models for hypersonic flows," *Progress in Aerospace Sciences*, vol. 42, no. 7, pp. 469 – 530, 2006.

[33] D. Lopez, D. D. Fernández, and J. Gonzalo, "Impact of turbulence modelling on external supersonic flow field simulations in rocket aerodynamics," *International Journal of Computational Fluid Dynamics*, vol. 27, no. 8-10, pp. 332–341, 2013.

[34] Y. Bazilevs, M. Hsu, J. Kiendl, R. Wüchner, and K. Bletzinger, "3D simulation of wind turbine rotors at full scale. Part II: Fluid – structure interaction modeling with composite blades," *International Journal for Numerical Methods in Fluids*, vol. 65, no. October 2010, pp. 236–253, 2011.

[35] Ü. Kaynak, "Supersonic boundary-layer transition prediction under the effect of compressibility using a correlation-based model," *Proceedings of the Institution of Mechanical Engineers, Part G: Journal of Aerospace Engineering*, vol. 226, no. 7, pp. 722–739, 2012.

[36] S. Saha and D. Chakraborty, "Hypersonic intake starting characteristics-A CFD validation study," *Defence Science Journal*, vol. 62, no. 3, pp. 147–152, 2012.

[37] L. Wang, Y. Zhao, and S. Fu, "Computational study of drag increase due to wall roughness for hypersonic flight," *The Aeronautical Journal*, vol. 121, no. 1237, pp. 395–415, 2017.

[38] J. Huang, J. V. Bretzke, and L. Duan, "Assessment of turbulence models in a hypersonic cold-wall turbulent boundary layer," *Fluids*, vol. 4, no. 1, 2019.

[39] L. Duan, I. Beekman, and M. P. Martín, "Direct numerical simulation of hypersonic turbulent boundary layers. Part 2. Effect of wall temperature," *Journal of Fluid Mechanics*, vol. 655, pp. 419–445, 2010.

[40] G. N. Coleman, J. Kim, and R. D. Moser, "A numerical study of turbulent supersonic isothermal-wall channel flow," *Journal of Fluid Mechanics*, vol. 305, p. 159–183, 1995.

[41] E. R. Shellabarger, *Computational characterization of shock wave - boundary layer interactions on flat plates and compression ramps in laminar, hypersonic flow*. Master's Thesis, Iowa State University, 2018.

[42] N. L. R. Center, "DNS: Supersonic/Hypersonic Zero-Pressure-Gradient Plate Flows." https://turbmodels.larc.nasa.gov/Other_DNS_Data/supersonic_hypersonic_flatplate.html. Accessed: 2020-11-09.

[43] N. Sahoo, V. Kulkarni, and R. K. Peetala, "Conjugate heat transfer study in hypersonic flows," *Journal of The Institution of Engineers (India): Series C*, vol. 99, pp. 151–158, Apr. 2018.

[44] V. Alexiades, G. Amiez, and P.-A. Gremaud, "Super-time-stepping acceleration of explicit schemes for parabolic problems," *Communications in Numerical Methods in Engineering*, vol. 12, no. 1, pp. 31–42, 1996.

[45] P. Dechaumphai, A. Wieting, and A. Pandey, "Fluid-thermal-structural interaction of aerodynamically heated leading edges," Tech. Rep. April, National Aeronautics and Space Administration (NASA), Hampton, Virginia, 1989.

[46] X. Zhao, Z. Sun, L. Tang, and G. Zheng, "Coupled flow-thermal-structural analysis of hypersonic aerodynamically heated cylindrical leading edge," *Engineering Applications of Computational Fluid Mechanics*, vol. 5, no. 2, pp. 170–179, 2011.

[47] P. Manna and D. Chakraborty, "Numerical investigation of conjugate heat transfer problems," *Journal of Aerospace Sciences & Technologies*, vol. 56, no. 3, 2004.

[48] E. Marineau, J. Schetz, and R. Neel, "Turbulent Navier-Stokes simulations of heat transfer with complex wall Temperature variations," *Journal of Thermophysics and Heat Transfer*, vol. 21, 07 2007.

[49] T. B. Gatski and J.-P. Bonnet, "Compressible Turbulent Flow," in *Compressibility, Turbulence and High Speed Flow (Second Edition)* (T. B. Gatski and J.-P. Bonnet, eds.), pp. 39 – 77, Oxford: Academic Press, second edition ed., 2013.

[50] D. C. Wilcox, *Turbulence Modeling for CFD (Third Edition) (Hardcover)*. Turbulence Modeling for CFD, DCW Industries, 01 2006.

[51] U. Frisch, *Turbulence: The legacy of A.N. Kolmogorov*. Cambridge University Press, 11 1995.

[52] F. G. Schmitt, "About Boussinesq's turbulent viscosity hypothesis: historical remarks and a direct evaluation of its validity," *Comptes Rendus - Mecanique*, vol. 335, no. 9-10, pp. 617–627, 2007.

[53] C. L. Rumsey, "Turbulence Modeling Resource." https://turbmodels.larc.nasa.gov/, June 2020. Accessed: 2020-11-09.

[54] D. C. Wilcox, "Multiscale model for turbulent flows," *AIAA Journal*, vol. 26, no. 11, pp. 1311–1320, 1988.

[55] S. Sarkar, G. Erlebacher, M. Y. Hussaini, and H. O. Kreiss, "The analysis and modelling of dilatational terms in compressible turbulence," *Journal of Fluid Mechanics*, vol. 227, no. June, pp. 473–493, 1991.

[56] F. R. Menter, "Two-equation eddy-viscosity turbulence models for engineering applications," *AIAA Journal*, vol. 32, no. 8, pp. 1598–1605, 1994.

[57] T. D. Economon, F. Palacios, S. R. Copeland, T. W. Lukaczyk, and J. J. Alonso, "Su2: An open-source suite for multiphysics simulation and design," *AIAA Journal*, vol. 54, no. 3, March 2016.

[58] F. M. White, *Viscous Fluid Flow (Third Edition)*. McGraw-Hill, 2006.

[59] F. R. Menter, "Zonal two equation k-w turbulence models for aerodynamic flows," in *23rd Fluid Dynamics, Plasmadynamics, and Lasers Conference*, July 1993.

[60] Siemens PLM Software Inc., "Simcenter STAR-CCM+ 2020.2 - User Guide." https://docs.sw.siemens.com/en-US/product/226870983/doc/PL20200617112215329.userGuide_html_2020, 2020. Accessed on 03.11.2020.

[61] F. Palacios, T. D. Economon, A. C. Aranake, S. R. Copeland, A. K. Lonkar, T. W. Lukaczyk, D. E. Manosalvas, K. R. Naik, A. Santiago Padrón, B. Tracey, A. Variyar, and J. J. Alonso, "Stanford university unstructured (SU2): Open-source analysis and design technology for turbulent flows," *52nd Aerospace Sciences Meeting*, pp. 1–33, 2014.

[62] C. Rumsey, "Turbulence modeling verification and validation (invited)," in *52nd AIAA Aerospace Sciences Meeting - AIAA Science and Technology Forum and Exposition*, 01 2014.

[63] C. L. Rumsey, "Turbulence Model Benchmarking Working Group." https://turbmodels.larc.nasa.gov/tmbwg.html, June 2020. Accessed: 2021-12-02.

[64] C. Hall, *Laws and Models: Science, Engineering, and Technology*. CRC Press, 10 2018.

[65] M. Wu and M. P. Martin, "Direct numerical simulation of supersonic turbulent boundary layer over a compression ramp," *AIAA Journal*, vol. 45, no. 4, pp. 879–889, 2007.

[66] D. Gregory-Smith, "Fundamentals of compressible flow," *International Journal of Heat and Fluid Flow*, vol. 4, pp. 181–182, 1983.

[67] J. van Oostrom, *Effects of increasing aerothermodynamic fidelity on hypersonic trajectory optimisation for flight testing purposes*. Master's thesis, Delft University of Technology, 2015.

[68] I. A. Hall, *Simulating scramjet behavior: Unstart Prediction in a supersonic, turbulent inlet-isolator duct flow*. Master's thesis, Purdue University, 2019.

[69] X.-s. Li, X.-d. Ren, and C.-w. Gu, "An Improved Roe Scheme for all Mach-number flows simultaneously curing known problems," *arXiv: Computational Physics*, 2017.

[70] L. F. G. Marcantonia, J. P. Tamagno, and S. a. Elaskar, "High Speed Flow Simulation Using OpenFOAM," *Asociacion Argentina de Mecánica Computacional*, vol. 31, pp. 2939–2959, 2012.

[71] A. Bukva, K. Zhang, N. Christopher, and J.-P. Hickey, "Assessment of turbulence modeling for massively-cooled turbulent boundary layer flows with transpiration cooling," *Physics of Fluids*, vol. 33, no. 9, p. 095114, 2021.

[72] A. Kurganov and E. Tadmor, "New high-resolution central schemes for nonlinear conservation laws and convection–diffusion equations," *Journal of Computational Physics*, vol. 160, no. 1, pp. 241 – 282, 2000.

[73] A. Kurganov, And Guergana, and P. Siam, "Semidiscrete central-upwind schemes for hyperbolic conservation laws and hamilton–jacobi equations," *J. Comput. Phys. SIAM J. Sci. Comput*, vol. 23, pp. 707–740, 01 2000.

[74] C. Greenshields, H. Weller, L. Gasparini, and J. Reese, "Implementation of semi-discrete, non-staggered central schemes in a colocated, polyhedral, finite volume framework, for high-speed viscous flows," *International Journal for Numerical Methods in Fluids*, vol. 63, pp. 1 – 21, 01 2009.

[75] S. Isaev and D. Lysenko, "Testing of numerical methods, convective schemes, algorithms for approximation of flows, and grid structures by the example of a supersonic flow in a step-shaped channel with the use of the cfx and fluent packages," *Journal of Engineering Physics and Thermophysics*, vol. 82, pp. 321–326, 03 2009.

[76] E. M. S. Ekanayake, *Numerical Simulation of a Convergent Divergent Supersonic Nozzle Flow*. Master's thesis, RMIT University, 2013.

[77] ANSYS, Inc., "ANSYS CFX-Solver Theory Guide." http://read.pudn.com/downloads500/ebook/2077964/cfx_thry.pdf, 2011. Accessed on 03.11.2020.

[78] R. J. Comstock, *Hypersonic heat transfer load analysis in STAR-CCM+*. Master's Thesis, California Polytechnic State University, 2020.

[79] P. G. Cross and M. R. West, "Simulation of hypersonic flowfields using STAR-CCM+," Tech. Rep. January, Naval Air Warfare Center Weapons Division, China Lake, CA, 2019.

[80] SU2, Multiphysics Simulation and Design Software, "User's guide." https://su2code.github.io/docs_v7/home/, 2020. Accessed on 03.11.2020.

[81] OpenCFD Ltd (ESI Group), "User guide." https://www.openfoam.com/documentation/user-guide/, 2016-2018. Accessed on 03.11.2020.

[82] Slater, John W., "Examining Spatial (Grid) Convergence." https://www.grc.nasa.gov/www/wind/valid/tutorial/spatconv.html, 2021. Accessed on 06.12.2021.

[83] T. Verstraete and R. Braembussche, "A novel method for the computation of conjugate heat transfer with coupled solvers," in *International Symposium on Heat Transfer in Gas Turbine Systems*, pp. 1–17, 01 2009.

[84] A. R. Wieting and M. S. Holden, "Experimental study of shock wave interference heating on a cylindrical leading edge at Mach 6 and 8," *AIAA 22nd Thermophysics Conference, 1987*, vol. 1987, 1987.

[85] Robert A. Braeunig, "Liquid oxygen & liquid hydrogen." http://www.braeunig.us/space/comb-OH.htm, 2008. Accessed on 11.11.2021.

[86] S. Corda, *Introduction to Aerospace Engineering with a Flight Test Perspective*. Wiley, 03 2017.

[87] G. N. Rao and N. R. Keshavan, "Axisymmetric turbulent boundary layers in zero pressure-gradient flows," *Journal of Applied Mechanics, Transactions ASME*, vol. 39, no. 1, pp. 25–32, 1972.

[88] ANSYS, Inc., "ANSYS FLUENT 12.0 User's Guide." https://www.afs.enea.it/project/neptunius/docs/fluent/html/ug/main_pre.htm, 2009. Accessed on 03.11.2020.

[89] D. Bose, J. L. Brown, D. K. Prabhu, P. Gnoffo, C. O. Johnston, and B. Hollis, "Uncertainty assessment of hypersonic aerothermodynamics prediction capability," *Journal of Spacecraft and Rockets*, vol. 50, no. 1, pp. 12–18, 2013.

[90] N. J. Georgiadis, D. A. Yoder, M. A. Vyas, and W. A. Engblom, "Status of turbulence modeling for hypersonic propulsion flowpaths," *Theoretical and Computational Fluid Dynamics*, vol. 28, no. 3, pp. 295–318, 2014.

[91] B. Launder and D. Spalding, "Mathematical models of turbulence," *Academic Press*, 1972.

[92] W. L. Oberkampf and T. G. Trucano, "Verification and validation in computational fluid dynamics," *Progress in Aerospace Sciences*, vol. 38, pp. 209–272, 2002.

[93] J. A. Freeman and C. J. Roy, "Verification and validation of reynolds-averaged navier–stokes turbulence models for external flow," *Aerospace Science and Technology*, vol. 32, no. 1, pp. 84 – 93, 2014.

[94] P. Spalart, "Trends in turbulence treatments," in *Fluids 2000 Conference and Exhibit*, (Denver, CO), AIAA, 2000.

[95] F. R. Menter, "Influence of freestream values on k-omega turbulence model predictions," *AIAA Journal*, vol. 30, no. 6, pp. 1657–1659, 1992.

[96] W. L. Oberkampf and F. G. Blottner, "Issues in computational fluid dynamics code verification and validation," *AIAA Journal*, vol. 36, no. 5, pp. 687–695, 1998.

[97] C. J. Roy, "Review of code and solution verification procedures for computational simulation," *Journal of Computational Physics*, vol. 205, no. 1, pp. 131 – 156, 2005.

[98] L. Fu, S. Bose, and P. Moin, "Heat transfer in three-dimensional intersecting shock-wave/turbulent boundary-layer interactions with wall-modeled large-eddy simulations," *arXiv: Computational Physics*, 2020.

[99] C. L. Rumsey, "Implementing turbulence models into the compressible RANS equations.." https://turbmodels.larc.nasa.gov/implementrans.html. Accessed: 2020-11-09.

[100] C. L. Rumsey, "SST-Vm Expected Results - 2D Zero Pressure Gradient Flat Plate." https://turbmodels.larc.nasa.gov/flatplate_sst.html, May 2021. Accessed: 2021-12-06.

[101] M. A. Dornheim, "Planetary flight surge faces budget realities," *Aviation Week & Space Technology*, vol. 145, no. 24, pp. 44–46, 1996.

[102] W. Terster, "Nasa considers switch to delta 2," *Space News*, vol. 8, no. 2, pp. 13–19, 1997.

[103] R. Peyret and T. D. Taylor, *Computational methods for fluid flow*. New York: Springer-Verlag, 2 ed., 1983.

[104] G. C. Oates, ed., *Aerothermodynamics of gas turbine and rocket propulsion*. AIAA Education Series, New York: AIAA, 1984.

[105] R. Volpe, "Techniques for collision prevention, impact stability, and force control by space manipulators," in *Teleoperation and Robotics in Space* (S. B. Skaar and C. F. Ruoff, eds.), Progress in Astronautics and Aeronautics, pp. 175–212, Washington, DC: AIAA, 1994.

[106] C. M. Thompson, "Spacecraft thermal control, design, and operation," in *AIAA Guidance, Navigation, and Control Conference*, vol. 1 of *CP849*, (Washington, DC), pp. 103–115, AIAA, 1989.

[107] Y. Chi, ed., *Fluid Mechanics Proceedings*, NASA SP-255, 1993.

APPENDICES

A - Supersonic Cold-Wall Flat Plate Results: Constant Temperature Wall B.C.

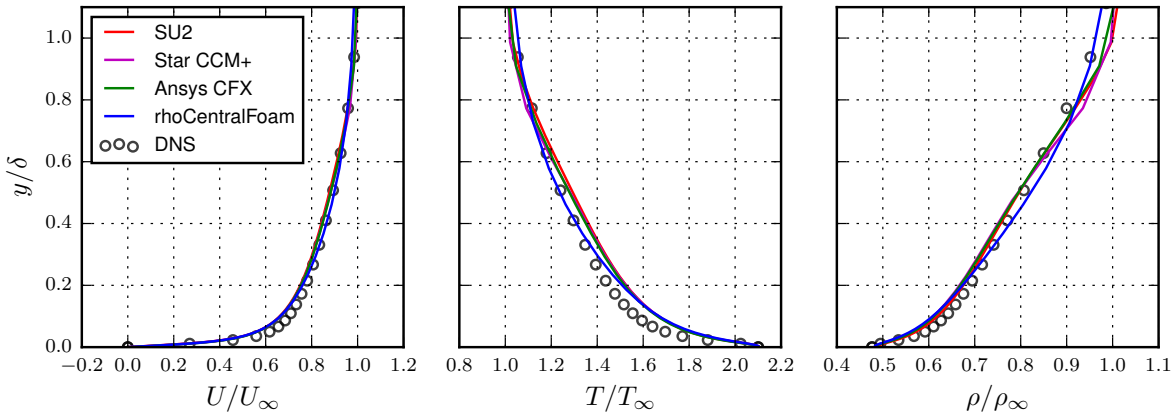

Figure A1: Normalized wall-normal properties for Mach 2.5 supersonic wedge with high wall cooling ($T_w/T_{aw} = 1$), compared to DNS at $Re_\theta = 2825$.

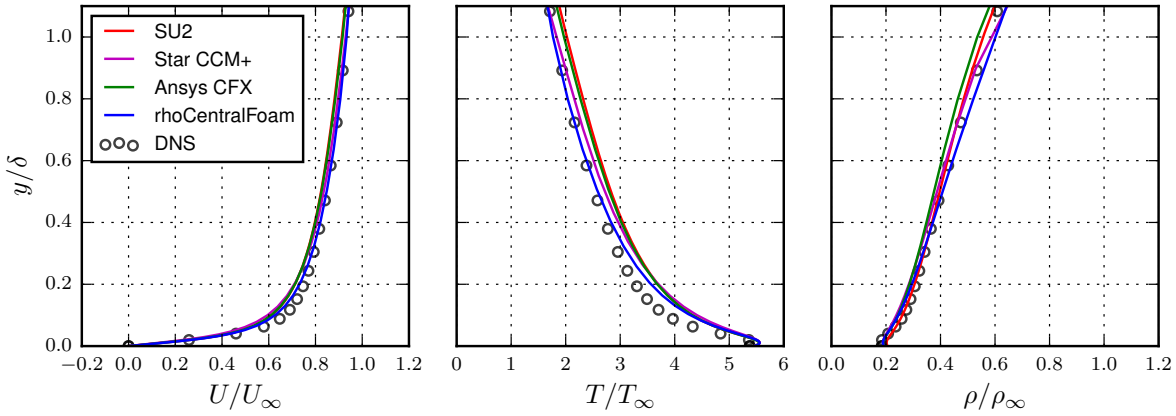

Figure A2: Normalized wall-normal properties for Mach 5.86 supersonic wedge with low wall cooling ($T_w/T_{aw} = 0.76$), compared to DNS at $Re_\theta = 9455$.

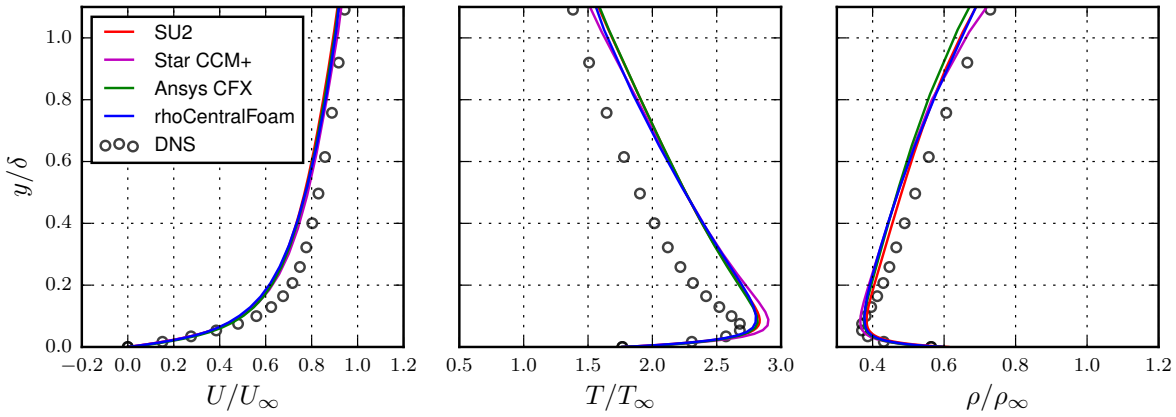

Figure A3: Normalized wall-normal properties for Mach 5.84 supersonic wedge with high wall cooling ($T_w/T_{aw} = 0.25$), compared to DNS at $Re_\theta = 2121$.

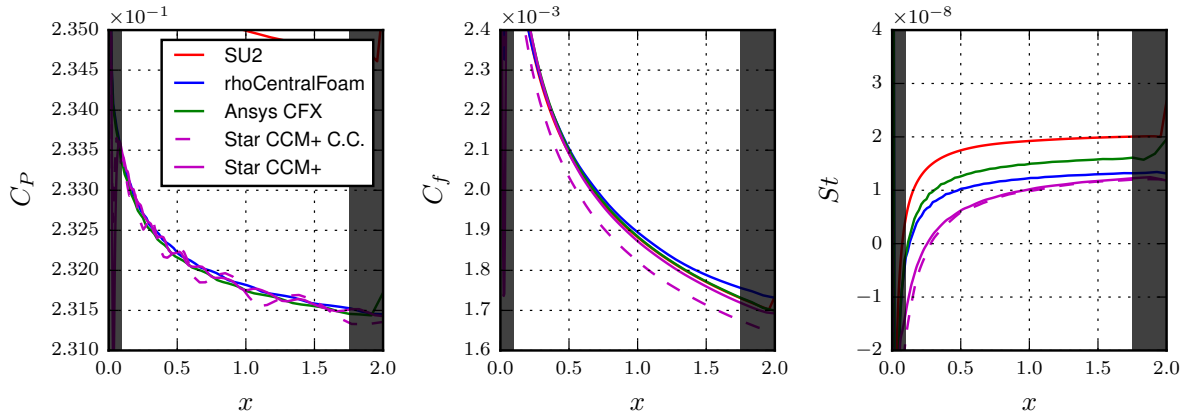

Figure A4: Coefficient of pressure, coefficient of skin friction drag, and wall heat flux for Mach 2.5 supersonic flat plate with no wall cooling ($T_w/T_{aw} = 1$). The red marker shows the corresponding Stanton number for the DNS case at $Re_\theta = 2825$. The dotted line shows the effect of Sarkar's compressibility correction in Star-CCM+.

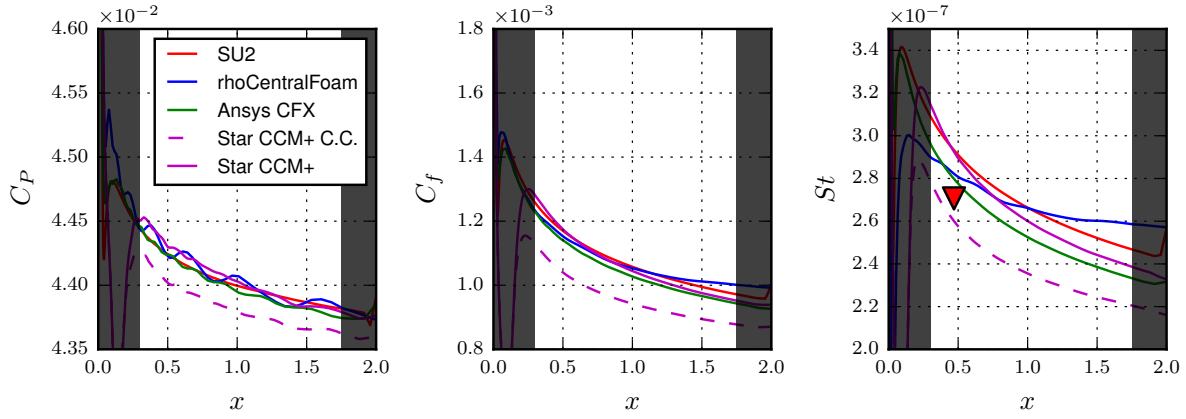

Figure A5: Coefficient of pressure, coefficient of skin friction drag, and wall heat flux for Mach 5.86 supersonic flat plate with low wall cooling ($T_w/T_{aw} = 0.76$). The red marker shows the corresponding Stanton number for the DNS case at $Re_\theta = 9455$. The dotted line shows the effect of Sarkar's compressibility correction in Star-CCM+.

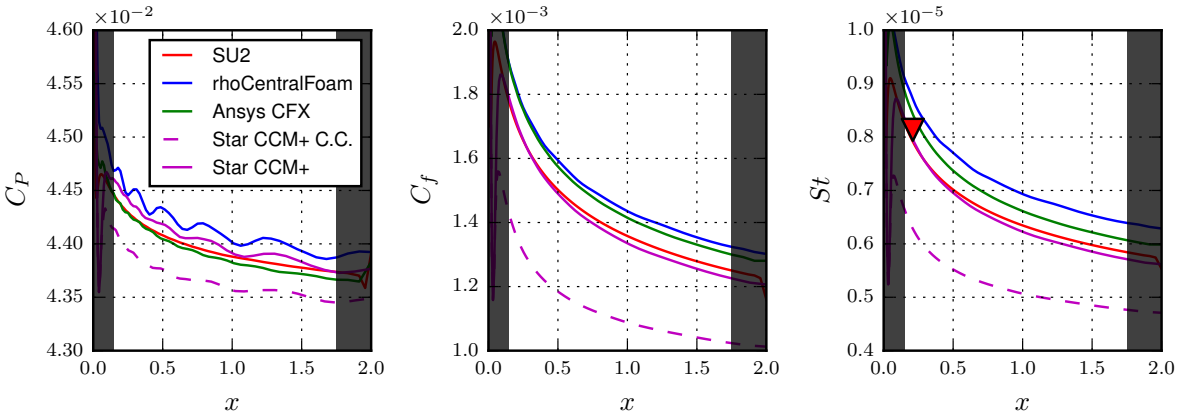

Figure A6: Coefficient of pressure, coefficient of skin friction drag, and wall heat flux for Mach 5.84 supersonic flat plate with high wall cooling ($T_w/T_{aw} = 0.25$). The dotted line shows the effect of Sarkar's compressibility correction in Star-CCM+.

B - Supersonic Cold-Wall Wedge Results: Constant Temperature Wall B.C.

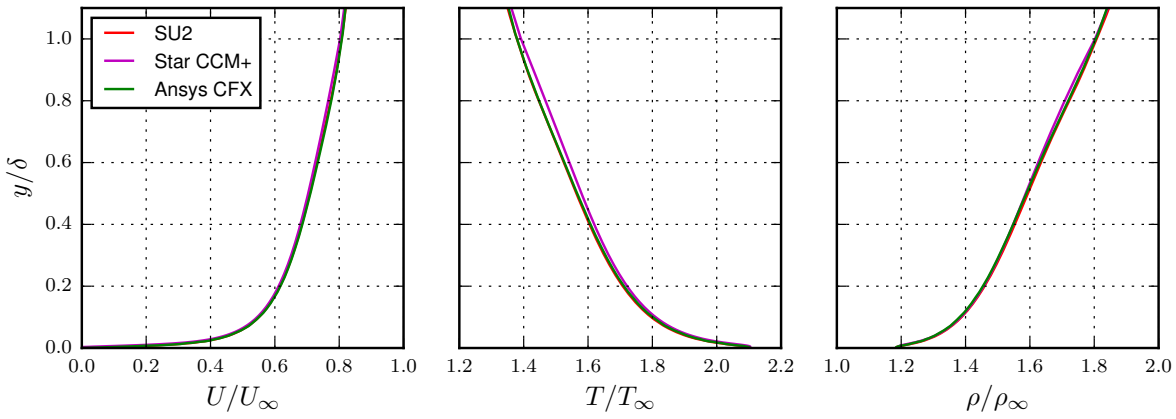

Figure B1: Normalized wall-normal properties for Mach 2.5 supersonic wedge with no wall cooling ($Tw/Taw = 1$).

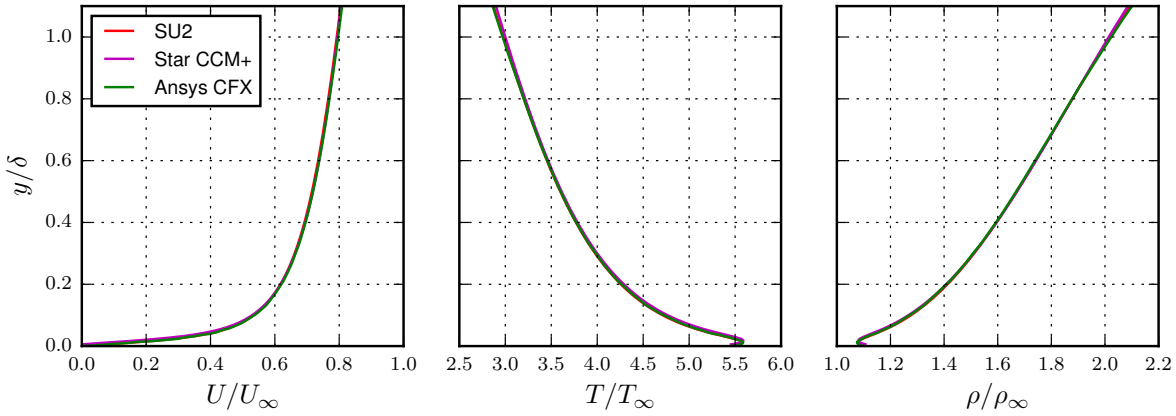

Figure B2: Normalized wall-normal properties for Mach 5.86 supersonic wedge with low wall cooling ($Tw/Taw = 0.76$).

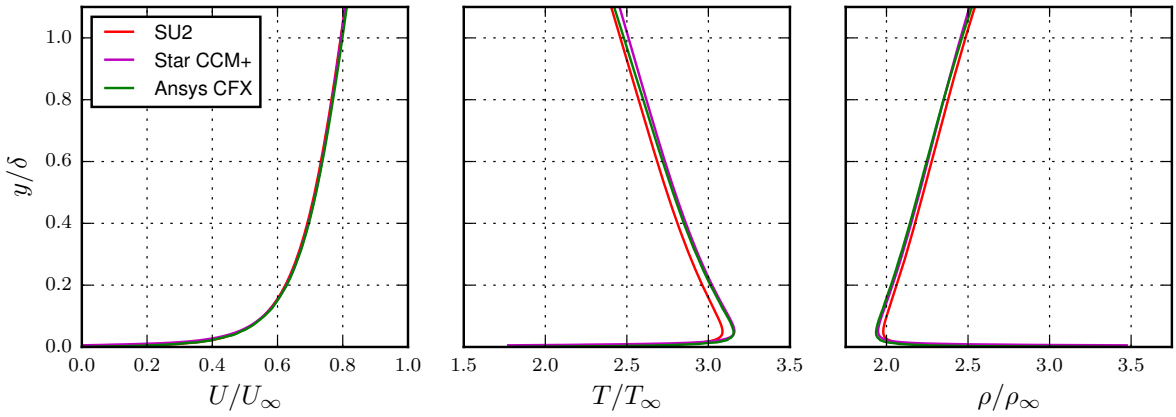

Figure B3: Normalized wall-normal properties for Mach 5.84 supersonic wedge with high wall cooling ($Tw/Taw = 0.25$).

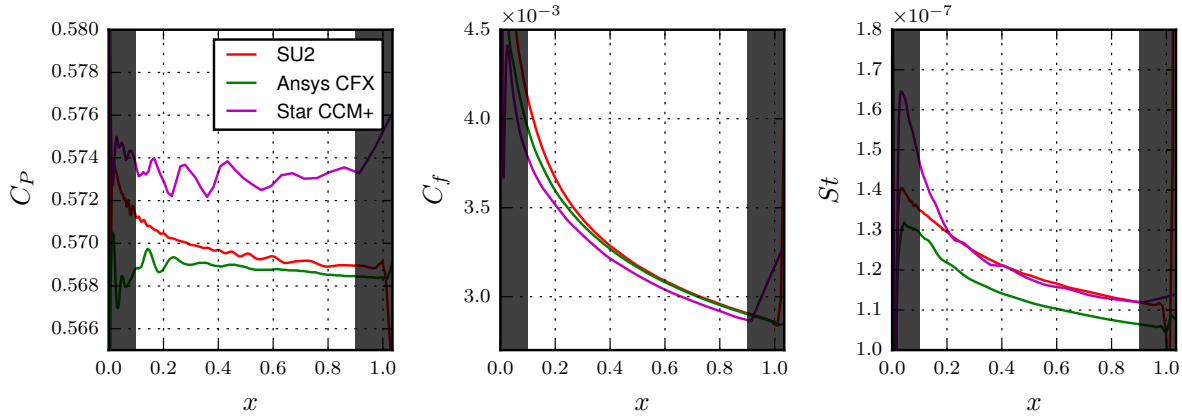

Figure B4: Coefficient of pressure, coefficient of skin friction drag, and wall heat flux for Mach 2.5 supersonic wedge with no wall cooling ($T_w/T_{aw} = 1$).

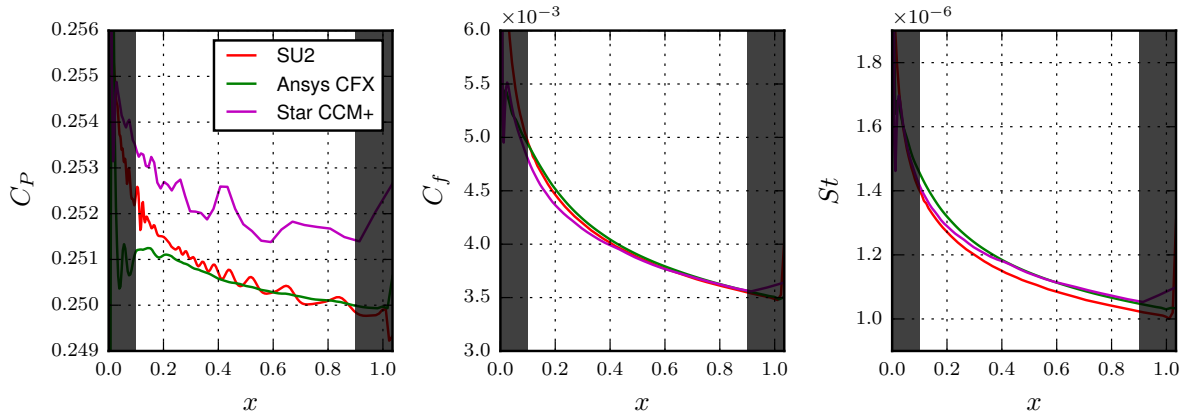

Figure B5: Coefficient of pressure, coefficient of skin friction drag, and wall heat flux for Mach 5.84 supersonic wedge with low wall cooling ($T_w/T_{aw} = 0.76$).

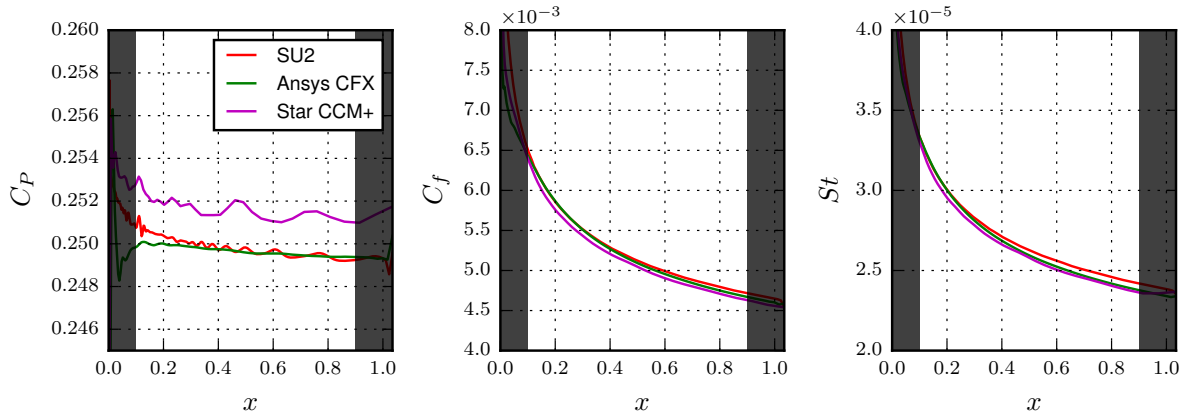

Figure B6: Coefficient of pressure, coefficient of skin friction drag, and wall heat flux for Mach 5.84 supersonic wedge with high wall cooling ($T_w/T_{aw} = 0.25$).

Table B1: Solver variation for a boundary layer on a wedge with a constant temperature wall.

Prop.	**Mach 2.5** $T_w/T_{aw} = 1$			**Mach 5.86** $T_w/T_{aw} = 0.75$			**Mach 5.84** $T_w/T_{aw} = 0.25$		
	Max. Abs.	**Max. Rel.**	**Avg. Rel.**	**Max. Abs.**	**Max. Rel.**	**Avg. Rel.**	**Max. Abs.**	**Max. Rel.**	**Avg. Rel.**
U/U_∞	4.71e-4	10.28%	4.37%	2.91e-4	3.75%	4.06%	2.33e-4	9.05%	3.75%
ρ/ρ_∞	1.13e-3	10.66%	4.47%	7.51e-4	4.13%	4.47%	8.66e-4	10.71%	4.12%
T/T_∞	9.74e-4	9.01%	3.54%	1.13e-3	2.78%	2.82%	6.81e-4	6.47%	2.78%
C_P	1.45e-2	3.25%	1.17%	6.94e-3	3.52%	1.53%	6.61e-3	3.36%	1.46%
C_f	1.56e-4	6.15%	2.51%	1.50e-4	4.86%	2.03%	2.10e-4	5.16%	2.15%
St	1.29e-8	14.74%	6.02%	3.74e-8	4.09%	1.55%	1.13e-6	5.39%	2.15%

C - Supersonic Cold-Wall Flat Plate Results: Constant Heat Flux B.C.

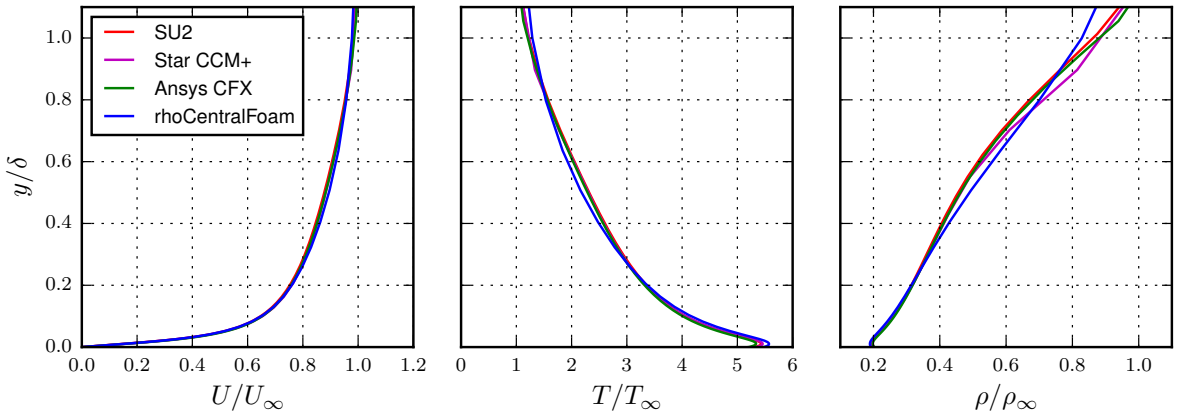

Figure C1: Normalized wall-normal properties for Mach 5.86 supersonic flat plate with low wall cooling with a constant heat flux boundary condition ($q_w = -2500 W/m^2$).

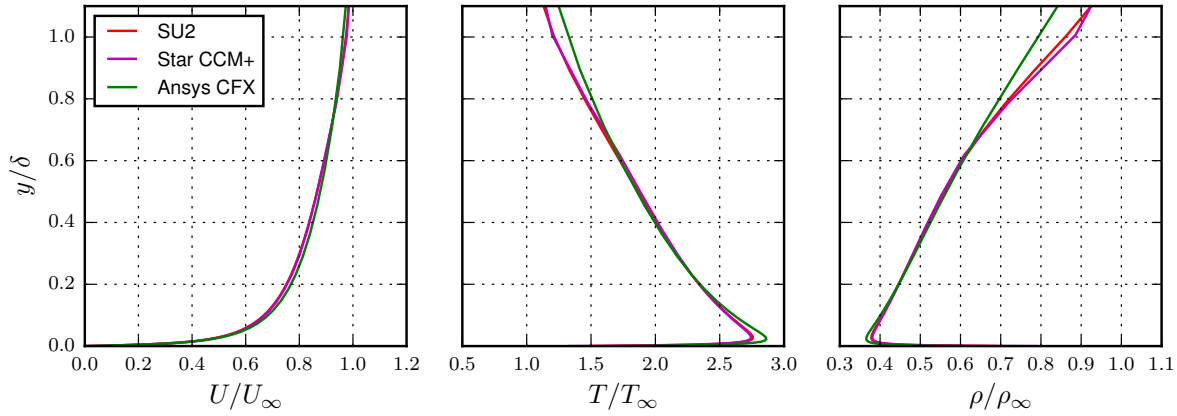

Figure C2: Normalized wall-normal properties for Mach 5.84 supersonic flat plate with high wall cooling with a constant heat flux boundary condition ($q_w = -1000W/m^2$).

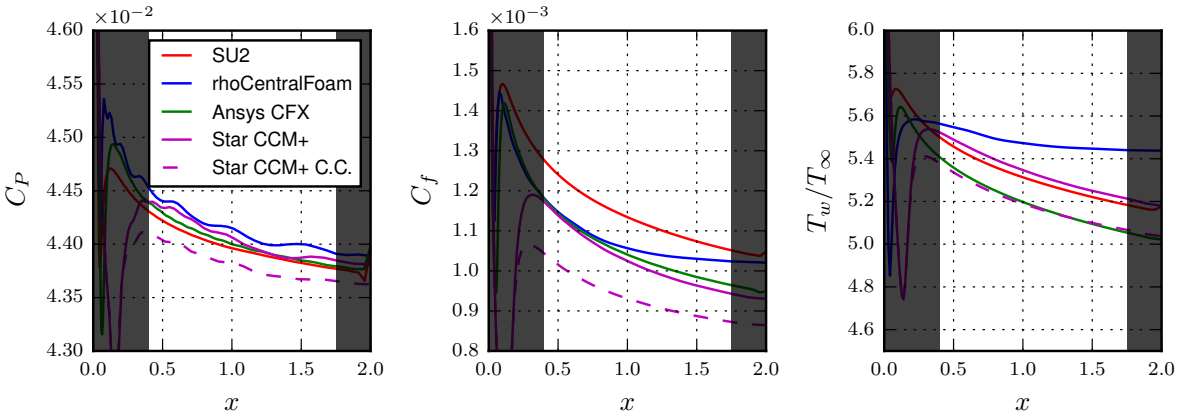

Figure C3: Coefficient of pressure, coefficient of skin friction drag, and normalized wall temperature for Mach 5.86 supersonic flat plate with low wall cooling ($q_w = -2,500W/m^2$).

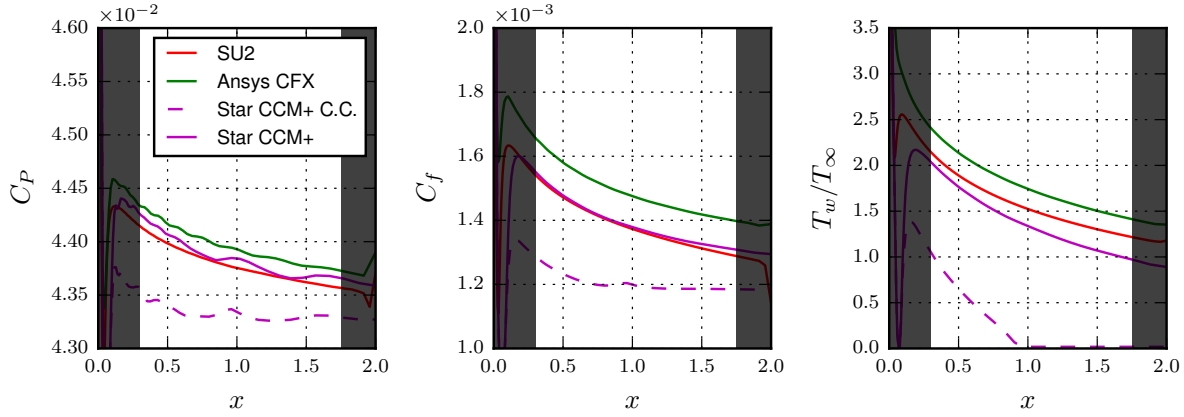

Figure C4: Coefficient of pressure, coefficient of skin friction drag, and normalized wall temperature for Mach 5.84 supersonic flat plate with high wall cooling ($q_w = -10000 W/m^2$).

Table C1: Solver variation for a boundary layer on a flat plate with a constant heat flux at the wall.

Prop.	**Mach 5.86** $St = 3E-7$			**Mach 5.84** $St = 7E-6$		
	Max. Abs.	**Max. Rel.**	**Avg. Relative**	**Max. Abs.**	**Max. Rel.**	**Avg. Rel.**
U/U_∞	2.50e-3	13.2%	3.60%	3.32e-3	16.65%	4.98%
ρ/ρ_∞	2.46e-3	15.70%	4.78%	3.46e-3	24.18%	7.54%
T/T_∞	2.40e-3	8.10%	2.52%	3.18e-3	6.19%	2.09%
c_P	3.19e-3	6.08%	1.83%	2.74e-3	5.18%	2.01%
c_f	1.94e-4	15.02%	4.38%	9.20e-5	5.48%	2.17%
T_w/T_∞	0.29	16.09%	1.68%	0.50	27.54%	9.74%